Predictability and Dynamics of Warm-Core Mesoscale Vortex Formation with the 8 May 2009 "Super Derecho" Event

CALEB T. GRUNZKE[a] AND CLARK EVANS

Atmospheric Science Program, Department of Mathematical Sciences, University of Wisconsin–Milwaukee, Milwaukee, Wisconsin

ABSTRACT

The predictability and dynamics of the warm-core mesovortex associated with the northern flank of the 8 May 2009 "super derecho" event are examined by coupling the Advanced Research Weather Research and Forecasting Model with the ensemble adjustment Kalman filter implementation within the Data Assimilation Research Testbed facility. Cycled analysis started at 1200 UTC 2 May 2009, with observations assimilated every 6 h until 1200 UTC 7 May 2009, at which time a 50-member ensemble of 36-h convection-allowing ensemble forecasts were launched. The ensemble forecasts all simulated a mesoscale convective system, but only 7 out of 50 members produced a warm-core mesovortex-like feature similar in intensity to the observed mesovortex.

Ensemble sensitivity and composite analyses were conducted to analyze the environmental differences between ensemble members. A more amplified upstream upper-level trough near the time of observed convection initiation is associated with a stronger simulated mesovortex. The amplification of the trough results in increases in the magnitudes of the low-level jet and thermal gradient. Consequently, more moisture is transported poleward into western Kansas, leading to earlier convection initiation in ensemble members with the strongest mesovortices. A circulation budget is performed on the ensemble members with the strongest (member 10) and weakest (member 5) time-averaged circulations. The ascending front-to-rear flow, descending rear-to-front flow, and divergent low-level flow of an MCS are more prominent in member 10, which is hypothesized to allow for the convergence of more background cyclonic absolute vorticity and, thus, facilitating the development of a stronger mesovortex.

1. Introduction

An intense mesoscale convective system (MCS) formed over northwestern Kansas in the morning hours of 8 May 2009. This MCS caused damaging, straight-line wind gusts of up to $50 \, \mathrm{m \, s^{-1}}$ and 26 tornadoes, of which 7 were of EF-2 or greater intensity on the enhanced Fujita (EF) scale (Coniglio et al. 2011). The "super derecho" (Weisman et al. 2013) resulted in an estimated $115 million in damage as it traveled from northwestern Kansas to the southern Appalachians (Evans et al. 2014). A unique characteristic about this MCS was that a strong, warm-core mesoscale vortex developed on its northern flank. Despite this unique occurrence, a numerical simulation performed in real time at the

National Center for Atmospheric Research (NCAR) was able to successfully forecast the observed event (Weisman et al. 2013). This and other studies (e.g., Melhauser and Zhang 2012; Snively and Gallus 2014; Xu et al. 2015a,b) have shown the capability of numerical models to provide skillful MCS forecasts in spite of imperfect initial conditions (ICs) and physical parameterization methods. It remains to be seen, however, if these skillful forecasts result from chance or instead suggest an appreciable amount of predictability exists for MCSs and their associated hazards.

Numerous studies have been conducted on the 8 May 2009 super derecho. Coniglio et al. (2011) examined the environment and initial transformation of the convective system. While synoptic forcing and instability were weak, a combination of mesoscale features allowed for convection initiation (CI) to occur. The collocation of high amounts of low-level moisture, steep midlevel lapse rates, and a strong low-level jet (LLJ) fostered an environment that allowed for convection to increase in

---

[a] Current affiliation: Cooperative Institute for Mesoscale Meteorological Studies, University of Oklahoma, Norman, Oklahoma.

Corresponding author e-mail: Clark Evans, evans36@uwm.edu

intensity and organize into a persistent MCS. The high-impact MCS occurred in an unusual environment compared to other similar events within the central United States. Though no individual characteristic of the environment was particularly atypical compared to those found in association with known derecho-producing environments (e.g., Coniglio et al. 2004, 2011), the combination of all such environmental characteristics was atypical (Evans et al. 2014).

Weisman et al. (2013) analyzed output from a high-resolution Advanced Research Weather Research and Forecasting Model (WRF-ARW; Skamarock et al. 2008) simulation that produced an accurate forecast of this event. The bow echo, as it matured, moved east into and through an environment of high most unstable convective available potential energy (MUCAPE) and strong vertical wind shear across the central plains. As the MCS subsequently moved into an environment characterized by weaker thermodynamic instability and vertical wind shear across eastern Kansas and Missouri, an intense, warm-core mesovortex developed on the northern end of the bow echo. Cyclonic vertical vorticity that was originally a deep strip along and immediately behind the leading line became consolidated on the southern edge of the northernmost cell.

The development of the warm-core mesovortex was studied further using a circulation budget and backward trajectory-based vorticity budget analyses (Evans et al. 2014). Vertical vorticity around the edges of the mesovortex was initially generated by updraft tilting and subsequent cyclonic amplification of environmental streamwise vorticity ahead of the MCS as well as downdraft tilting and subsequent anticyclonic amplification of baroclinically generated crosswise vorticity within the MCS's cold pool. The mesovortex's lower-tropospheric rotation increased due to the consolidation of the cyclonic vertical vorticity via large-scale convergence and expulsion of anticyclonic vertical vorticity by the diffluent descending rear inflow jet within the system's cold pool.

Xu et al. (2015a) conducted a high-resolution WRF-ARW simulation to examine the genesis of two mesovortices within the convective system's leading line. The vertical vorticity of the mesovortices formed from near-surface horizontal vorticity that was tilted into the vertical, with surface friction argued to create the near-surface horizontal vorticity. Xu et al. (2015b) subsequently argued that the downward pressure perturbation force associated with the mesovortices near the bow echo apex caused the rear-inflow jet to descend to the surface and locally enhance the surface winds.

Several studies have been conducted into the predictability of MCS events with respect to short-range initial condition uncertainty. Wandishin et al. (2008, 2010) sought to quantify the amount of confidence a forecaster could have in 1–2-day forecasts of MCS occurrence. Initial condition uncertainty at the level of current 24-h forecast errors resulted in an idealized MCS forecast success rate of 70%. Only reducing the uncertainties of all perturbed variables (wind speed, relative humidity, and instability) to below the level of observational uncertainty resulted in substantial improvements in MCS forecast success rate. Durran and Weyn (2016) generated a 25-member numerical model ensemble to study error growth dynamics and predictability of idealized squall lines. Downscale error growth from the synoptic scale was argued to be more important than upscale growth from small-scale errors, particularly for lead times greater than 3–4 h.

Output from a 40-member WRF-ARW convection-allowing ensemble initialized with the initial conditions obtained from an ensemble Kalman filter implementation within a state-of-the-art cycled data assimilation system was utilized by Melhauser and Zhang (2012) to study the practical and intrinsic predictability at a 6–24-h lead time of the 9–10 June 2003 squall line and bow echo event. The study found that differences in weighted ICs that were well below the magnitude of observational uncertainty resulted in a bimodal forecast distribution. In general, while reducing the IC uncertainty can have a positive effect on the accuracy of a forecast, a bifurcation point can be reached in some cases at which point no further gains from reducing IC uncertainty can be made. It is unclear, however, as to whether these results are specific to the case studied or can be generalized to more MCS events.

Researchers have also examined MCS predictability by evaluating forecasts produced from different ensemble configurations. Lawson and Gallus (2016) studied the predictability of bow echoes, a subset of squall lines, using multiple ensemble prediction system configurations, including IC/lateral boundary condition (LBC) perturbations, microphysics parameterization variation, the stochastic kinetic energy backscatter scheme implementation within WRF-ARW of Berner et al. (2011), and a combination of the previous two. Of these configurations, IC uncertainty and variability were found to have the most influence on MCS positioning while model error exerted the most control on storm mode for the two cases considered. Additionally, numerous other studies have researched MCS predictability (e.g., Hohenegger et al. 2006; Hawblitzel et al. 2007; Hohenegger and Schar 2007; Adams-Selin et al. 2013; Schumacher et al. 2013; Durran and Gingrich 2014; and Peters and Roebber 2014, among others).
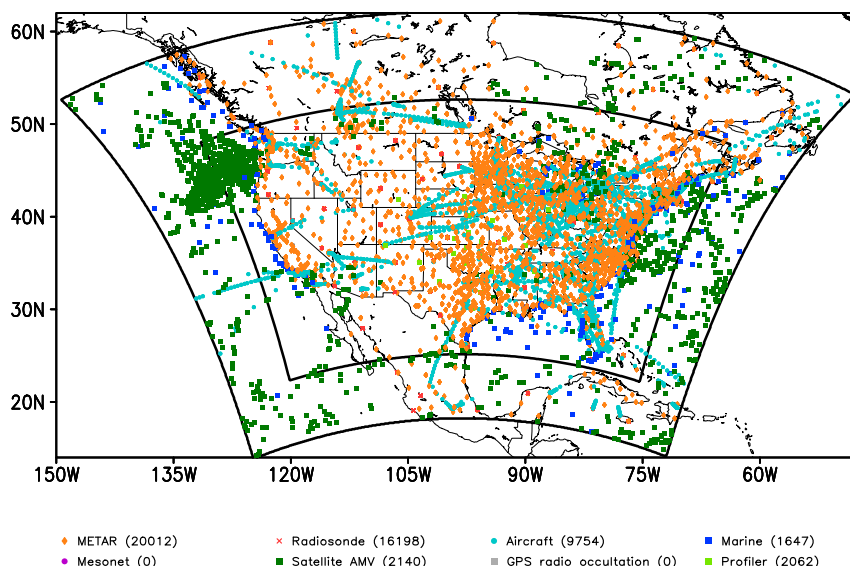
FIG. 1. Spatial distribution of assimilated observation platforms for the 1200 UTC 7 May 2009 analysis cycle. Observation counts are for unique observations within each platform type. The thick black lines indicate the domain configuration for the cycled analysis and free forecasts. Cycled analysis is conducted on the outer domain while the free forecasts utilize both domains.

The objectives of this research are to determine the predictability and better understand the dynamics of the 8 May 2009 super derecho. We want to determine if NWP models are capable of providing an accurate forecast of this and, by extension, other high-impact MCS(s) a day in advance. To do this, the WRF-ARW numerical model and ensemble adjustment Kalman filter (EAKF, or here EnKF; Anderson 2001), the latter as implemented within the Data Assimilation Research Testbed (DART; Anderson et al. 2009), are used. This state-of-the-art data assimilation technique allows for continuous cycling data assimilation for a specified number of intervals before launching ensemble forecasts. The purpose of this system is to generate ICs that provide ensemble perturbations comparable to or better than those of current operational ensemble modeling systems. Romine et al. (2013) and Schwartz et al. (2015b) discovered that more skillful convection-permitting forecasts resulted when forecasts were provided with WRF-DART analysis ICs rather than from a Global Forecast System (GFS) analysis during the first 12 h. The experimental design is discussed further in section 2. Section 3 contains the results and a discussion. Last, a summary and discussion is presented in the final section.

2. Methodology

a. Cycled analysis

DART (lanai release, rev. 8336), as coupled with WRF-ARW version 3.7.1 (Skamarock et al. 2008), is utilized to assimilate observations and generate ensemble ICs via an EnKF. Cycled data assimilation begins at 1200 UTC 2 May 2009 and continues every 6 h until 1200 UTC 7 May 2009, at which time 50-member ensemble forecasts (described in section 2b) are launched. Assimilation is conducted on a domain centered over the conterminous United States that extends into Canada, Mexico, and the Atlantic and Pacific Oceans (Fig. 1). It has 15-km horizontal grid spacing with 415×325 grid points and 50 vertical levels. Model parameterizations largely follow Romine et al. (2013, 2014) and are described in Table 1.

To generate ICs at the outset of the cycled assimilation experiment, the 1200 UTC 2 May 2009 GFS analysis is perturbed via 50 random samples of the National Centers for Environmental Prediction (NCEP) background error covariance matrix (Barker et al. 2012). LBCs for each data assimilation cycle are provided by 0-h GFS analyses and 6-h GFS forecasts perturbed using the fixed covariance perturbation technique of Torn et al. (2006). Adaptive Gaspari–Cohn localization (Gaspari and Cohn 1999; Anderson 2012), sampling error correction (Anderson 2012), and time- and space-varying adaptive prior inflation (Anderson 2009) are applied to the assimilation to decrease spurious correlations due to sampling errors and preserve ensemble spread (e.g., Torn 2010; Romine et al. 2013; Schwartz et al. 2014). Table 2 provides more information about the DART setup.

An example of assimilated observations for a representative assimilation cycle is provided in Fig. 1. Assimilated observations include standard aviation routine

TABLE 1. WRF-ARW Model options.

Parameter	Cycled analysis	Forecasts	References
Horizontal grid	415×325 $\Delta x = 15$ km	1581×1001 $\Delta x = 3$ km	
Vertical grid	50 levels $p_{top} = 50$ hPa	Same	
Cumulus parameterization	New Tiedtke	None	Tiedtke (1989) Zhang et al. (2011)
Boundary layer parameterization	Mellor–Yamada–Janjić (MYJ)	Same	Janjić (1994)
Microphysical parameterization	Thompson	Same	Thompson et al. (2008)
Longwave radiation	Rapid Radiative Transfer Model for Global Climate Models (RRTMG)	Same	Iacono et al. (2008)
Shortwave radiation	RRTMG	Same	Iacono et al. (2008)
Land surface parameterization	Noah	Same	Chen and Dudhia (2001)

weather reports [METARs; u, v, T, altimeter (Alt), specific humidity (q)], mandatory level rawinsondes and dropsondes (u, v, T, Alt, q), marine stations (u, v, T, Alt, q), aircraft (ACARS; u, v, T, q), profilers (u, v, pressure), atmospheric motion vectors (AMVs; u, v; Velden et al. 2005), and global positioning system (GPS) radio occultation refractivity (Kursinski et al. 1997). AMVs were processed by and obtained from the Cooperative Institute for Meteorological Satellite Studies (CIMSS). The GPS data were processed by and obtained from the Constellation Observing System for Meteorology, Ionosphere, and Climate. All other observations were obtained from the NCEP Meteorological Assimilation Data Ingest System. Table 3 provides a complete list of observations types, assumed observation errors, and observation windows. Model variables updated during cycled analysis include U, V, W, T, T2, QVAPOR, Q2, QCLOUD, QRAIN, QNRAIN, QSNOW, QICE, QNICE, QGRAUP, H_DIABATIC, REFL_10CM, PH, MU, V10, U10, and PSFC. Soil state is updated with soil data from the corresponding 0-h GFS analysis after data assimilation but before the next model advance.

Additional observation processing included the following: (i) the observational error was increased within five grid points of the domain's lateral boundaries (Romine et al. 2013); (ii) surface observations were excluded when the station height and model terrain differed by more than 300 m (Romine et al. 2013); (iii) observations that fell more than three standard deviations outside of the ensemble prior estimate were rejected (e.g., Romine et al. 2013); and (iv) the distance thresholds for aircraft and satellite-derived observations for wind were changed to ± 22.5 km and ± 25 hPa in the horizontal and vertical, respectively, to "superob" densely packed observations (Ha and Snyder 2014).

b. Free forecasts

Ensemble forecasts start at 1200 UTC 7 May 2009, run for 36 h, and are conducted on a two-way nested

domain. The outer domain is described in the previous section while the inner domain has 1580×1000 horizontal grid points with 3-km grid spacing and 50 vertical levels (Table 1). It is centered inside the cycled analysis domain and covers the conterminous United States (Fig. 1). The results of this study focus exclusively on output from the inner domain. A 50-member ensemble forecast is conducted using ICs provided by the cycled analysis system described in section 2a. LBCs are updated every 3 h using data provided by the 1200 UTC 7 May 2009 forecast cycle of the NCEP GFS model and perturbed using the fixed covariance perturbation technique of Torn et al. (2006). The frequency of model output is hourly. Physical parameterizations employed by the ensemble forecasts are identical to those described for the cycled analysis system except that convection on the forecast domain is treated explicitly (without parameterization; Table 1). This configuration is consistent with numerous studies that used DART coupled with WRF-ARW to generate WRF-ARW ensembles of skillful convection-allowing forecasts

TABLE 2. DART options.

Parameter	Value
Filter type	Ensemble adjustment Kalman filter
Adaptive inflation	True—initial 1.0, 0.8 (mean, spread)
Adaptive localization threshold	2000
Localization type	Gaspari–Cohn
Horizontal localization half-width	635 km
Vertical localization half-width	8 km
Outlier threshold	3.0
Ensemble members	50
Sampling error correction	True
Assimilation interval	6 h

TABLE 3. Assimilated observation types, assumed observation errors, and observation windows.

Platform	Variable	Observation error	Observation window (h)
METAR	Temperature	Ha and Snyder (2014)	±1
	E–W, N–S winds	Ha and Snyder (2014)	±1
	Specific humidity	Schwartz et al. (2015a)	±1
	Altimeter	NCEP statistics	±1
Radiosonde	Temperature	Schwartz et al. (2015b)	±1
	E–W, N–S winds	Romine et al. (2013, 2014)	±1
	Specific humidity	Schwartz et al. (2015a)	±1
	Surface altimeter	NCEP statistics	±1
Dropsonde	Temperature	NCEP statistics	±1
	E–W, N–S winds	NCEP statistics	±1
	Specific humidity	NCEP statistics	±1
	Surface altimeter	NCEP statistics	±1
Marine	Temperature	NCEP statistics	±1
	E–W, N–S winds	NCEP statistics	±1
	Specific humidity	Schwartz et al. (2015a)	±1
	Altimeter	NCEP statistics	±1
ACARS (22.5 km, 25 hPa)[a]	Temperature	NCEP statistics	±1
	E–W, N–S winds	NCEP statistics	±1
	Specific humidity	Schwartz et al. (2015a)	±1
Profiler	E–W, N–S winds	NCEP statistics	±1
	Pressure	NCEP statistics	±1
Satellite derived (22.5 km, 25 hPa)[a]	E–W, N–S winds	Romine et al. (2013)	±1
GPS	RO refractivity	Kuo et al. (2004)	±1

[a] Superobs (horizontal, vertical).

(e.g., Romine et al. 2013, 2014; Schwartz et al. 2014, 2015b,c; Torn and Romine 2015).

c. Ensemble sensitivity analysis

Results from the ensemble simulations are analyzed using the ensemble-based sensitivity analysis (ESA) of Ancell and Hakim (2007) and Torn and Hakim (2008). In this method, for a given ensemble size M, the sensitivity of the ensemble-mean value of a forecast metric **J** to a change in an analysis state variable **x** is determined by the covariance of **J** and **x** divided by the variance of **x**. The equation below denotes a linear regression between the forecast metric **J** and the analysis state variable **x**:

$$\frac{\partial J}{\partial x} = \frac{\text{cov}(\mathbf{J}, \mathbf{x})}{\text{var}(\mathbf{x})}. \quad (1)$$

The forecast metric **J** is a $1 \times M$ ensemble estimate. There are $N \times M$ ensemble estimates for any given state variable **x**, where N is equal to the number of horizontal grid points over the model domain. Both **J** and **x** have their ensemble means removed. The right-hand side of (1) is multiplied by the standard deviation of **x**, such that a one standard deviation change in **x** is responsible for a given change in **J**. ESA has been successfully employed in several recent studies to gain insight into deep, moist convection and related phenomena (e.g., Weisman et al. 2015; Torn and Romine 2015; Bednarczyk and Ancell

2015). Herein, the forecast metric **J** is the maximum 850-hPa circulation over a 1° × 1° area ($m^2 s^{-1}$) associated with the warm-core mesovortex at 1200 UTC 8 May 2009. Qualitatively similar results were obtained for ensemble
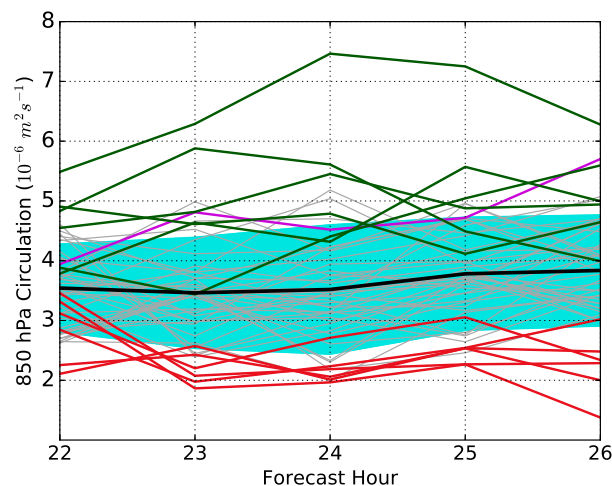

FIG. 2. 850-hPa circulation (associated with the mesovortex) time series for the 50 ensemble members between 1000 and 1400 UTC 8 May 2009. The ensemble mean is denoted by the thick, black line, teal shading above (below) the ensemble mean denotes less than (greater than) one standard deviation above (below) the ensemble mean, STRONG composite members (1, 10, 13, 15, 16, and 26) are denoted by green lines, WEAK composite members (5, 7, 18, 19, 28, and 36) are denoted by red lines, all other members are denoted by gray lines, and the hourly time series of 850-hPa circulation from Evans et al. (2014) is denoted by the purple line.

estimates of **J** at other forecast times from 1000 to 1400 UTC 8 May 2009 (not shown).

d. Composites

To facilitate comparison of synoptic and mesoscale environments between ensemble members with the strongest and weakest mesovortices, the six ensemble members with the strongest and weakest circulations from 1000 to 1400 UTC 8 May 2009 are utilized to create strong (STRONG) and weak (WEAK) composites, respectively. To determine composite membership, the ensemble mean plus and minus one standard deviation of the circulation data from all ensemble members were found (Fig. 2). Ensemble members one standard deviation above (below) the ensemble mean for at least two out of the five time steps were considered for STRONG (WEAK). If more than six qualified ensemble members existed, the six ensemble members with the strongest (weakest) circulations were utilized for STRONG (WEAK). Rapid Update Cycle (RUC; Benjamin et al. 2004) analyses were employed as "truth" to compare the composites to the "observed" environment.

e. Circulation budget analysis

To further examine differences in mesovortex evolution between the strongest (member 10) and weakest (member 5) time-averaged circulations, a circulation budget analysis is used. These two members were selected as representatives of their respective composites. From Evans et al. (2014), the equation utilized to calculate the change in circulation around an arbitrarily shaped closed region on an isobaric surface is given by

$$\frac{\partial C}{\partial t} = -\overline{f}\tilde{\delta}A - \overline{\varsigma}\tilde{\delta}A - \oint \varsigma' \mathbf{v}' \cdot \mathbf{n}\, dl + \oint \omega \left(\mathbf{k} \times \frac{\partial \mathbf{v}}{\partial p} \right) \cdot \mathbf{n}\, dl. \tag{2}$$

Overbars (tildes) signify the mean value around (within) the perimeter of the arbitrarily closed region. The local perturbation of a variable from its mean value about the perimeter of the closed region is denoted by a prime (e.g., $\mathbf{v}'$). The divergence of the wind components inside the closed region is signified by $\tilde{\delta}$. The term A represents the closed region's two-dimensional area on an isobaric surface, $\mathbf{n}$ denotes the unit vector locally normal and outward to the chosen closed region's horizontal boundary, $\mathbf{v}$ is the horizontal velocity vector, and $\oint$ represents the line integral about the edge of the closed region. All other variables' standard meteorological definitions are unchanged. Friction is neglected in this formulation.

For the right-hand side, the forcing terms represent the mean transport of mean planetary vorticity, mean transport of mean relative vorticity, eddy transport of perturbation relative vorticity, and tilting, respectively. Alternatively, the mean transport terms can be interpreted as the stretching of mean planetary vorticity and the stretching of mean relative vorticity, respectively. Further explanation of this equation and its interpretation is provided by Evans et al. (2014). The wind field utilized within the calculation of the circulation budget is storm relative. This is critical for the eddy transport term as it is highly sensitive to the storm motion estimate. An instantaneous, nonconstant storm-motion estimate (rounded to the nearest meter per second) is employed to calculate the storm-relative wind field, following Evans et al. (2014).

A square box with a side length equal to 100 km is employed to compute the circulation tendency. The control box is centered on the subjectively tracked vortex center of the circulation maximum associated with the mesovortex on the northern flank of the convective system at each analysis time. The simulated mesovortex in Evans et al. (2014) and in the STRONG members were found to exhibit minimal tilt with height (not shown). The control box utilized herein follows the methodology of Evans et al. (2014) and does not tilt with height. Following Davis and Galarneau (2009) and Evans et al. (2014), an ensemble of 121 boxes is employed at each analysis time. The boxes are placed ± 1 grid point with a range of ± 5 grid points in the x–y directions from the chosen center. All of the terms in the circulation budget are computed for each box and then are averaged over the 121 boxes. Budget calculations are completed between 0600 and 1500 UTC 8 May 2009 with a history interval of 15 min. All computations are done between 900 and 400 hPa ($\Delta p = 25$ hPa), and centered finite differencing is utilized for all partial derivatives.

3. Results and discussion

a. Data assimilation performance

For all surface observation platforms, root-mean-square error (RMSE), total spread, and bias are reduced for the posterior compared to the prior at each analysis time and do not amplify over time (Fig. 3). RMSE and total spread for a majority of the platforms are also nearly equal by the final cycled analysis time that, from Houtekamer and Mitchell (1998) and Dowell et al. (2004), enables for reasonably accurate forecast error covariance statistics to be derived and used in the assimilation process. The results closely match those of Romine et al. (2013; cf. our Fig. 3 to their Fig. 6) with slightly reduced RMSE and total spread for temperature, zonal wind, and meridional wind (Figs. 3a,d,e). A cool and slight moist bias is also evident (Figs. 3a,b);
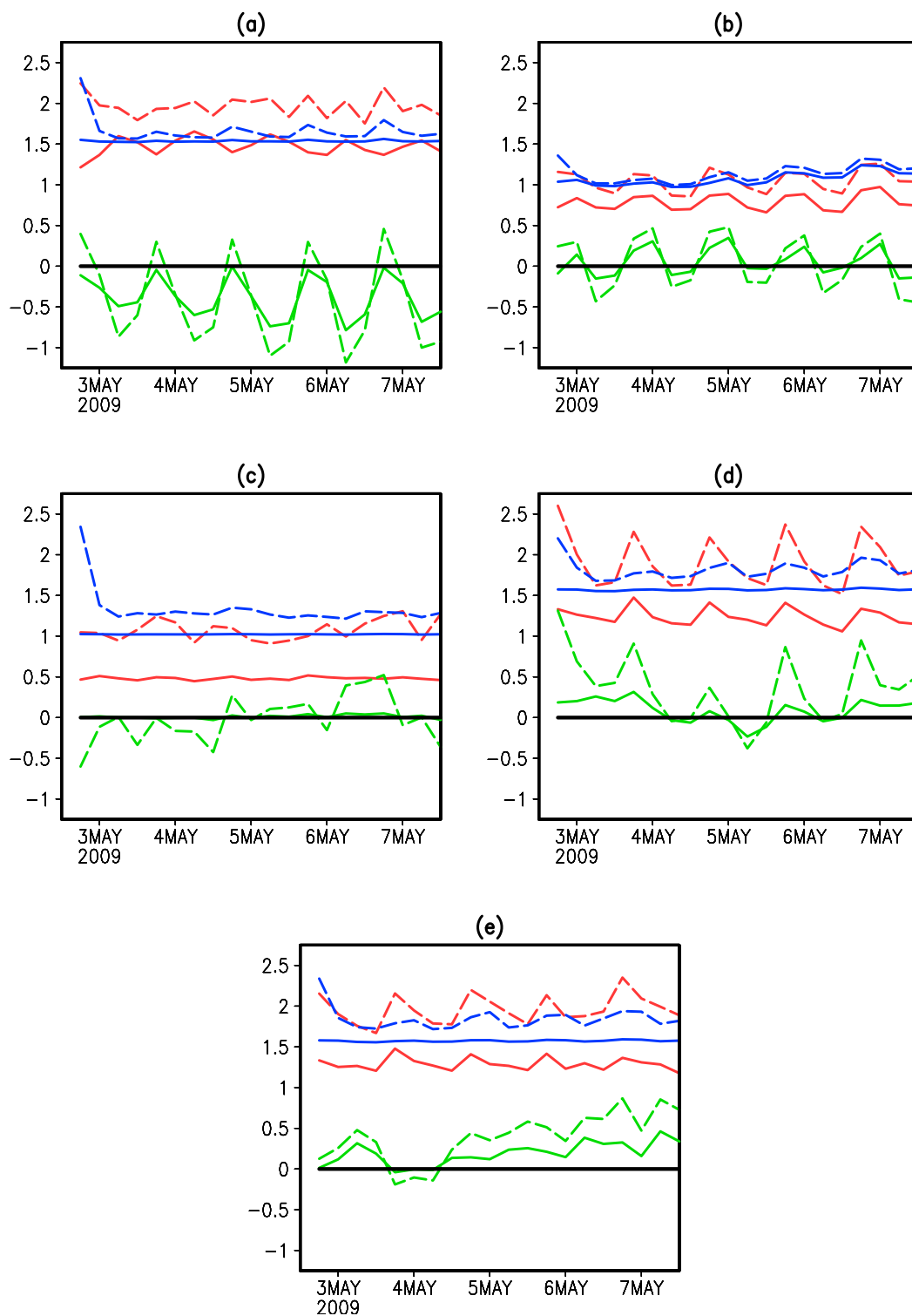
FIG. 3. RMSE (red), total spread (blue), and bias (green) of the prior (dashed) and posterior (solid) ensemble estimates for METAR (a) temperature (K), (b) specific humidity (g kg^{-1}), (c) altimeter (hPa), (d) u (m s^{-1}), and (e) v (m s^{-1}) observations between 1200 UTC 2 May and 1200 UTC 7 May 2009.
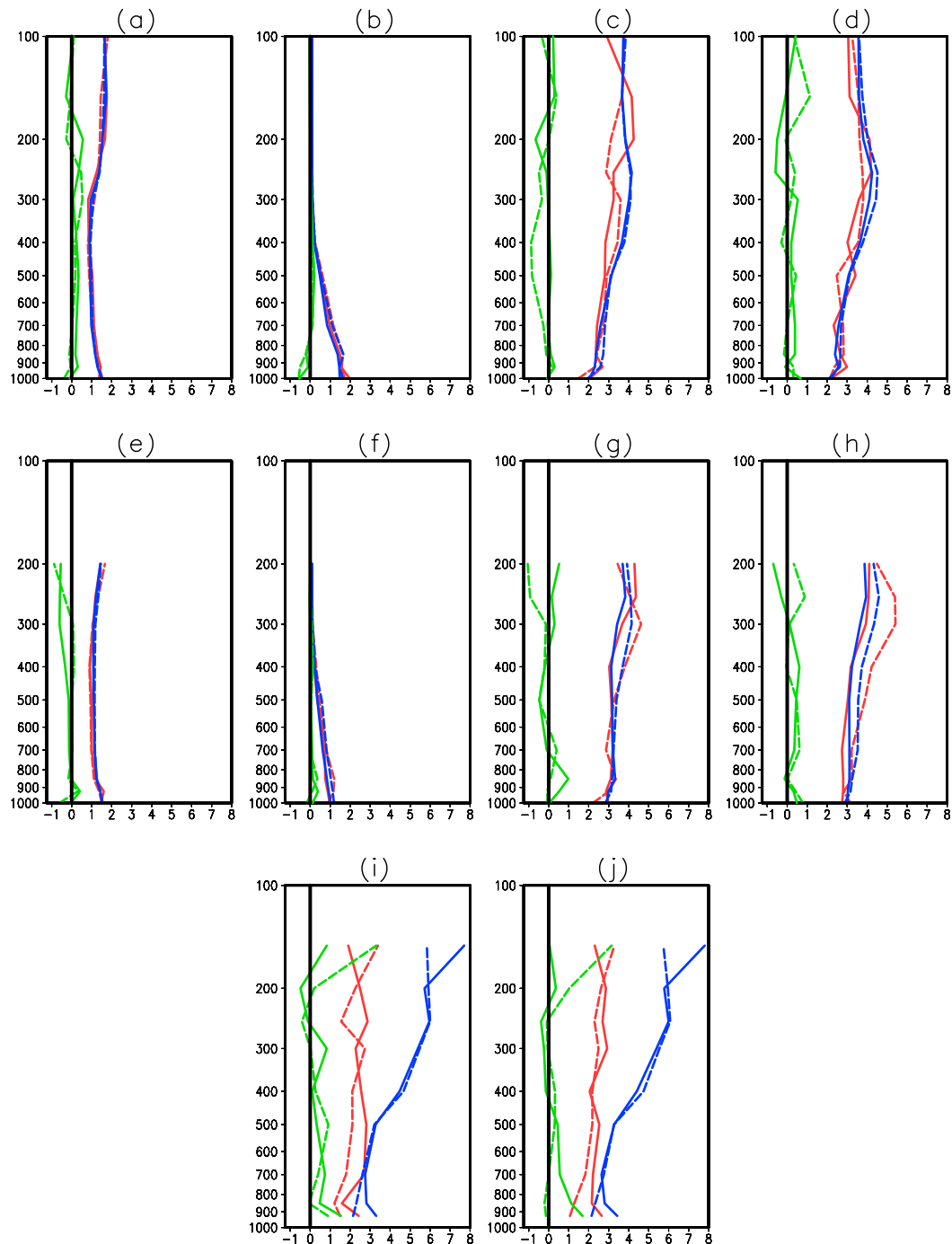
FIG. 4. RMSE (red), total spread (blue), and bias (green) of the posterior ensemble analysis at 0000 UTC 5 May 2009 (solid) and 1200 UTC 7 May 2009 (dashed) for radiosonde (a) temperature (K), (b) specific humidity (g kg^{-1}), (c) u wind (m s^{-1}), and (d) v wind (m s^{-1}); ACARS (e) temperature (K), (f) specific humidity (g kg^{-1}), (g) u wind (m s^{-1}), and (h) v wind (m s^{-1}); and AMV (i) u wind (m s^{-1}), and (j) v wind (m s^{-1}).

however, the biases are temporally out of phase with each other. It is thus unclear whether these biases are reflective of the MYJ's well-known cool/moist bias in preconvective boundary layers (e.g., Coniglio et al. 2013). Additionally, a slight easterly (northerly) bias is present in the 10-m zonal (meridional) wind (Figs. 3d,e).

Vertical profile observation platforms show similar performance to the surface platforms (Fig. 4). Most
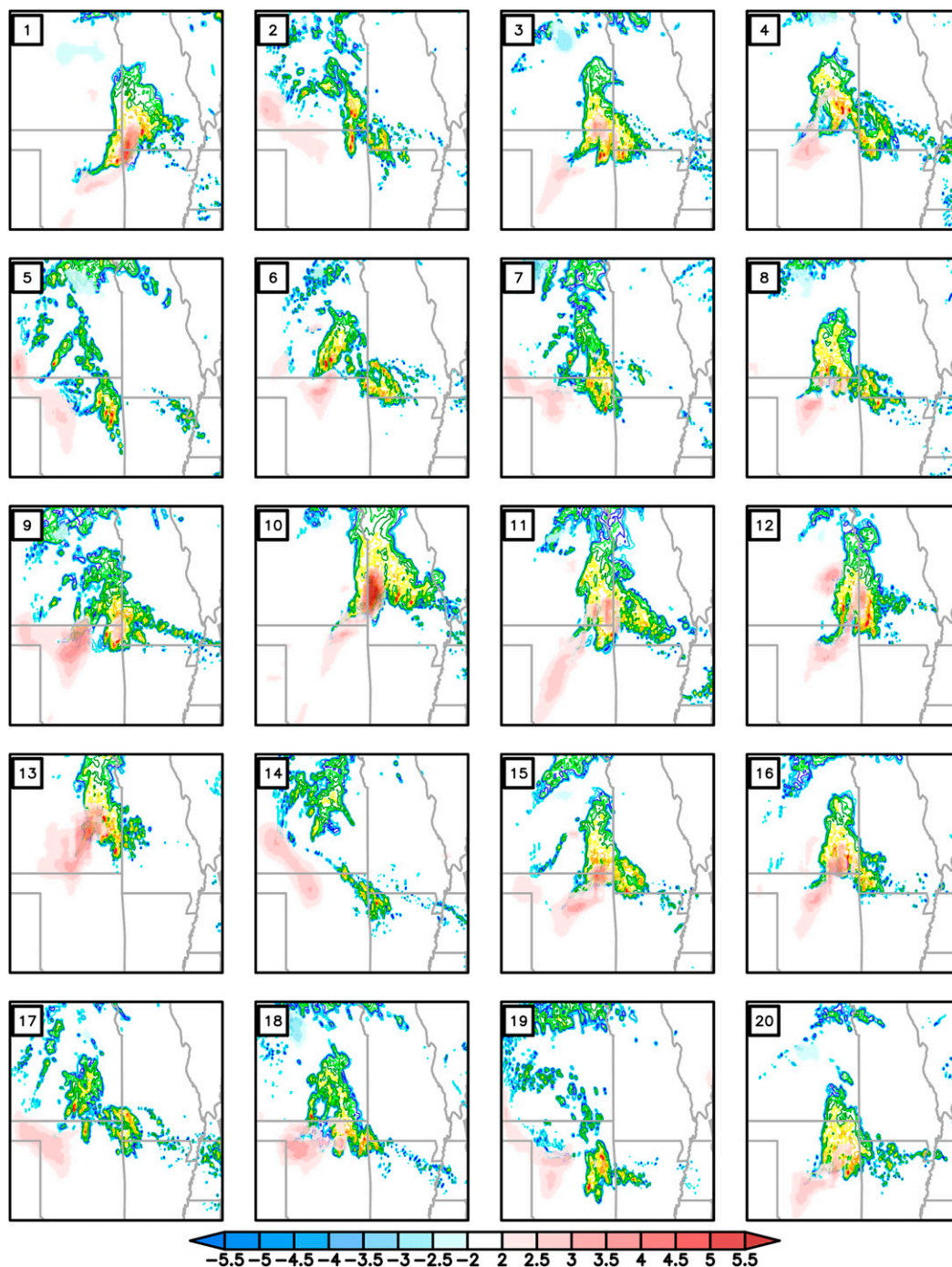
FIG. 5. 850-hPa circulation calculated over $1° \times 1°$ boxes centered at each model grid point (color shaded; $\times 10^6\,\mathrm{m^2\,s^{-1}}$) overlaid on 1-km AGL derived reflectivity (color contoured every 5 dBZ starting at 5 dBZ) for ensemble members 1–20 at 1200 UTC 8 May 2009.

variables across the platforms have good agreement between RMSE and total spread, signifying well-tuned observation error statistics, with near-zero bias consistent with Romine et al. (2013). However, satellite AMVs (Figs. 4i,j) have a large total spread relative to

RMSE. Assumed errors for the CIMSS AMVs are greater than Romine et al. (2013, 2014), although assimilation is explicitly limited to CIMSS AMVs with a CIMSS quality control value of <3 [akin to the error specification in Romine et al. (2013, 2014)]. Thus,
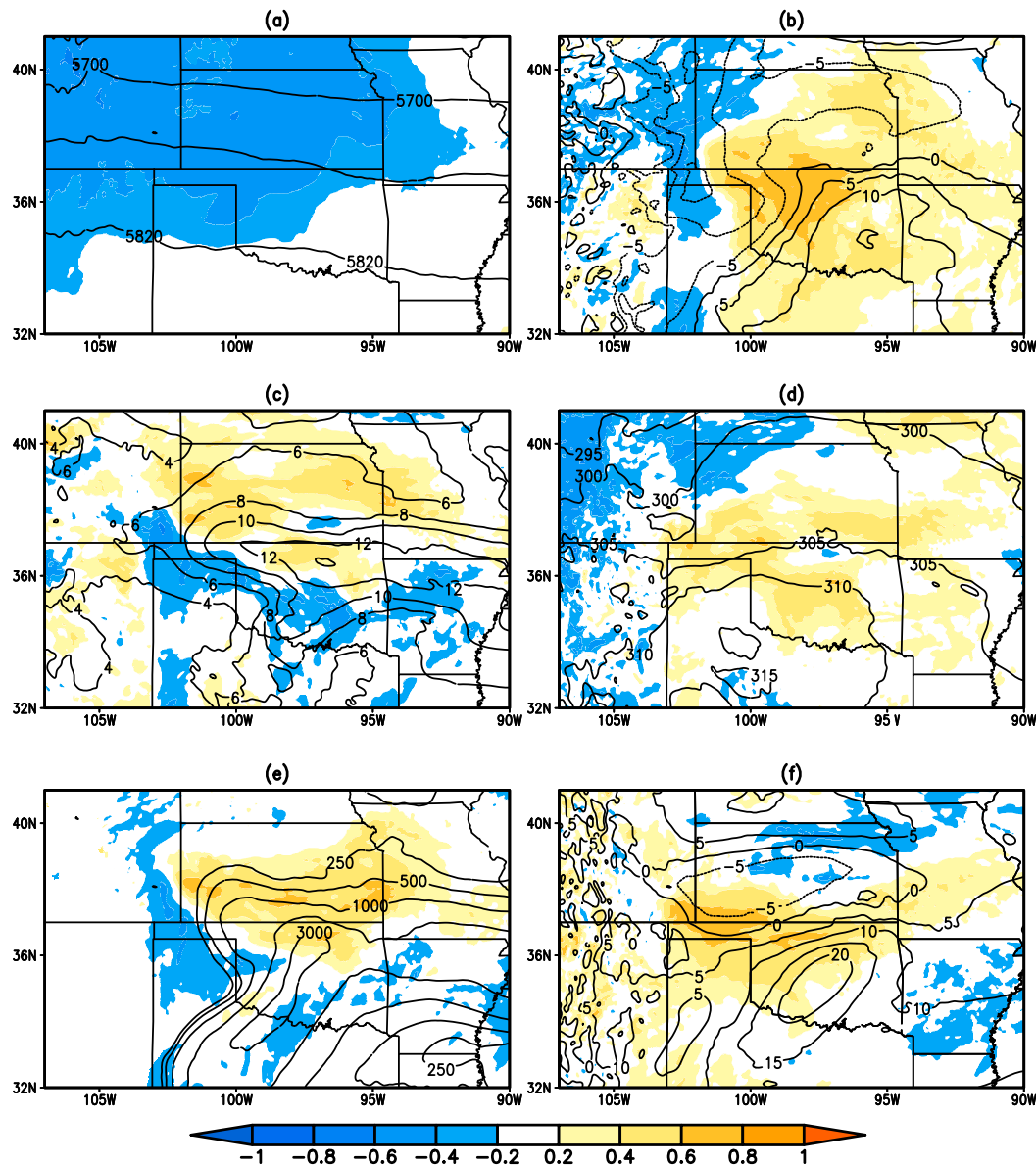
FIG. 6. Ensemble sensitivity analysis for (a) 500-hPa geopotential height (m; $\mathbf{x}$), (b) 850-hPa v wind (kt; $\mathbf{x}$), (c) 850-hPa specific humidity (g kg^{-1}; $\mathbf{x}$), (d) 850-hPa potential temperature (K; $\mathbf{x}$), (e) MUCAPE (J kg^{-1}; $\mathbf{x}$), and (f) 850-hPa u wind (kt; $\mathbf{x}$) at 0600 UTC 8 May 2009 with respect to 850-hPa maximum circulation ($\times 10^6$ m^2 s^{-1}; $\mathbf{J}$) at 1200 UTC 8 May 2009. Black contours denote the ensemble mean, while color shading denotes the sensitivity metric $\partial J / \partial x$. Warm colors denote a positive relationship between $\mathbf{J}$ and $\mathbf{x}$, while cool colors denote a negative relationship between $\mathbf{J}$ and $\mathbf{x}$.

assimilation performance could be improved through improved specification of assumed height-dependent AMV observation errors in DART. Given the typical spatial distribution of AMV observations (Fig. 1), this would improve analysis quality primarily over water near the cycled analysis domain boundaries and, thus, regions of greatest lateral boundary condition influence.

To evaluate how posterior ensemble analysis error compares to that of operational numerical weather prediction systems, 0.5° GFS analysis error relative to DART-assimilated observations is evaluated at each of the 20 assimilation times. GFS analysis quality statistics exhibit an overall worse performance for both the surface and vertical observation platforms at all cycled analysis times (not shown). However, it is important to
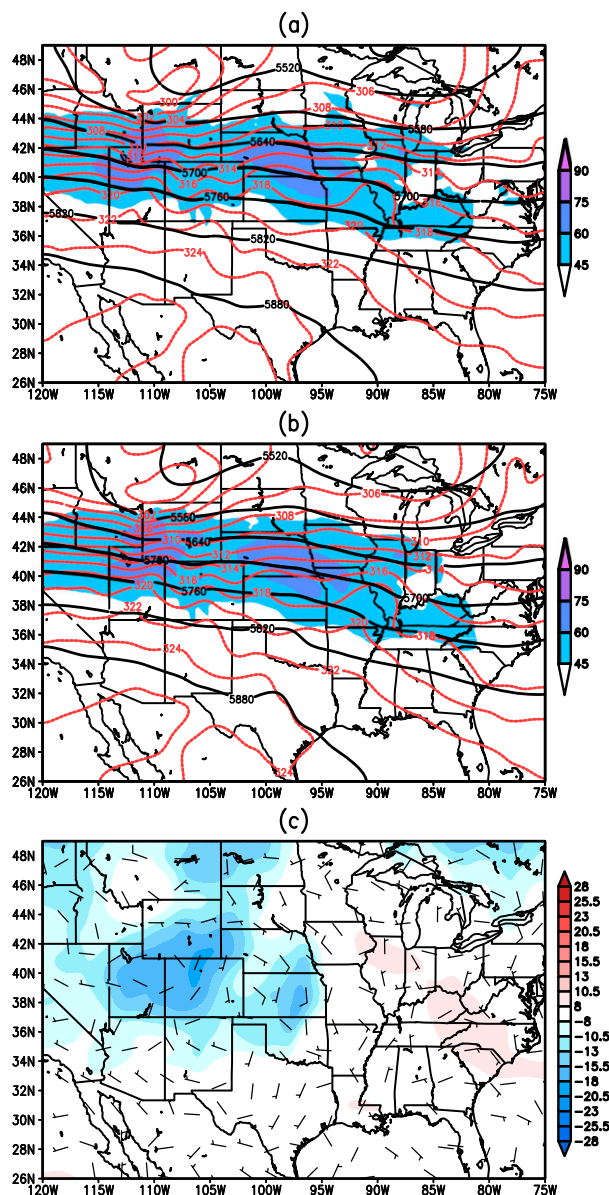
FIG. 7. 500-hPa total wind (kt, color shaded), 500-hPa geopotential height (m, black contours), and 500-hPa potential temperature (K, red dashed) at 0600 UTC 8 May 2009 for (a) STRONG and (b) WEAK. (c) STRONG − WEAK with 500-hPa geopotential height (m, color shaded) and 500-hPa total wind (half barb: 5 kt, full barb: 10 kt, pennant: 50 kt) at 0600 UTC 8 May 2009.

FIG. 8. 850-hPa total wind (color shaded in kt per color bar; barbs with half barb: 5 kt, full barb: 10 kt, pennant: 50 kt), 850-hPa geopotential height (m, black contours), and 850-hPa potential temperature (K, red dashed) at 0600 UTC 8 May 2009 for (a) STRONG and (b) WEAK.

confidence to the utility of the ensemble analyses generated herein for the study for the selected case.

b. Ensemble performance

Hourly 1-km above ground level (AGL) simulated reflectivity was first plotted for all ensemble members as a preliminary assessment of the ensemble members' MCS evolution and intensity compared to the observed event. Each member initiates a MCS somewhere in Kansas that travels eastward with time (Fig. 5). However, a few members (e.g., members 1, 10, 13, and 16) simulate a large, strong, and well-organized MCS with large area-averaged 850-hPa absolute vorticity while others (e.g., members 2, 5, 14, and 17) are much less organized and weaker. The location of the MCSs between members also varies, as stronger members are generally poleward of the weaker members.

The mesolow associated with the observed mesovortex had a surface pressure minimum of 8 hPa relative to the environmental pressure (Weisman et al. 2013). Mean sea level pressure (not shown) was analyzed

remember three things: the GFS input data are of coarser resolution than the WRF-DART assimilation system; the data assimilated between the two systems are not identical; and the numerical models used for the cycled analysis for each system are not identical. Thus, the GFS analysis assimilation performance is considered to be a worst-case scenario compared to the WRF-DART ensemble. Nevertheless, these statistics lend
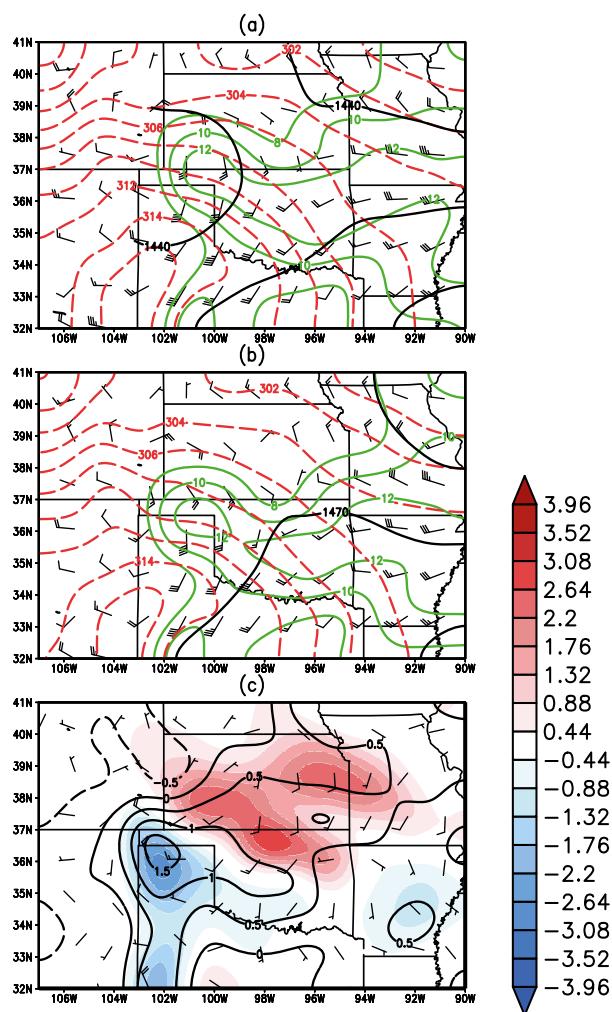
FIG. 9. 850-hPa total wind (half barb: 5 kt, full barb: 10 kt, pennant: 50 kt), 850-hPa geopotential height (m, black contours), potential temperature (K, red dashed), and specific humidity (g kg^{-1}, green contours) at 0600 UTC 8 May 2009 for (a) STRONG and (b) WEAK. (c) STRONG − WEAK with 850-hPa specific humidity (g kg^{-1}, color shaded), 850-hPa total wind (half barb: 5 kt, full barb: 10 kt, pennant: 50 kt), and 850-hPa potential temperature (K, black solid/dashed) at 0600 UTC 8 May 2009.

hourly from 1100 UTC 8 May to 1700 UTC 8 May 2009 to determine if any ensemble members produced a pressure minimum of similar intensity to the observed mesovortex. Only 7 out of 50 ensemble members produced a mesovortex surface pressure minimum of 4 hPa, while only 1 member exceeded the 8-hPa difference observed in Weisman et al. (2013). The ensemble's results display a high practical predictability of MCS occurrence over the central United States, consistent with previous studies (e.g., Wandishin et al. 2008, 2010; Peters and Roebber 2014), but a low practical predictability of mesovortex occurrence and intensity.
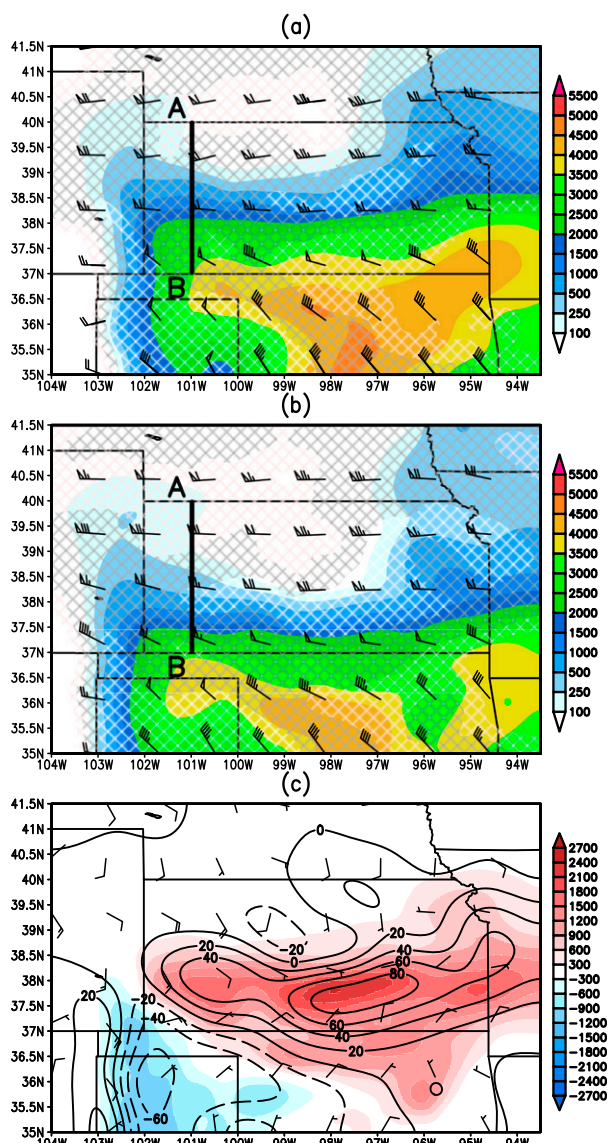
FIG. 10. MUCAPE (J kg^{-1}, color shaded), MUCIN [J kg^{-1}, gray hatched (white: −100 J kg^{-1}, light gray: −25 J kg^{-1}, dark gray: −10 J kg^{-1})], and 0–6-km wind shear (half barb: 5 kt, full barb: 10 kt, pennant: 50 kt) at 0600 UTC 8 May 2009 for (a) STRONG and (b) WEAK. Thick, black line drawn from A–B on (a) and (b) denotes vertical cross section in Fig. 14. (c) STRONG − WEAK with MUCAPE (J kg^{-1}, color shaded), MUCIN (J kg^{-1}, black solid/dashed), and 0–6-km wind shear (half barb: 5 kt, full barb: 10 kt, pennant: 50 kt) at 0600 UTC 8 May 2009.

c. Ensemble sensitivity analysis

From a synoptic-scale viewpoint, the 850-hPa circulation associated with the mesovortex at 1200 UTC 8 May 2009 is sensitive to the upstream 500-hPa trough around 6 h before 1200 UTC 8 May 2009 (Fig. 6a). Note that results for both analysis and forecast metrics at other surrounding forecast times
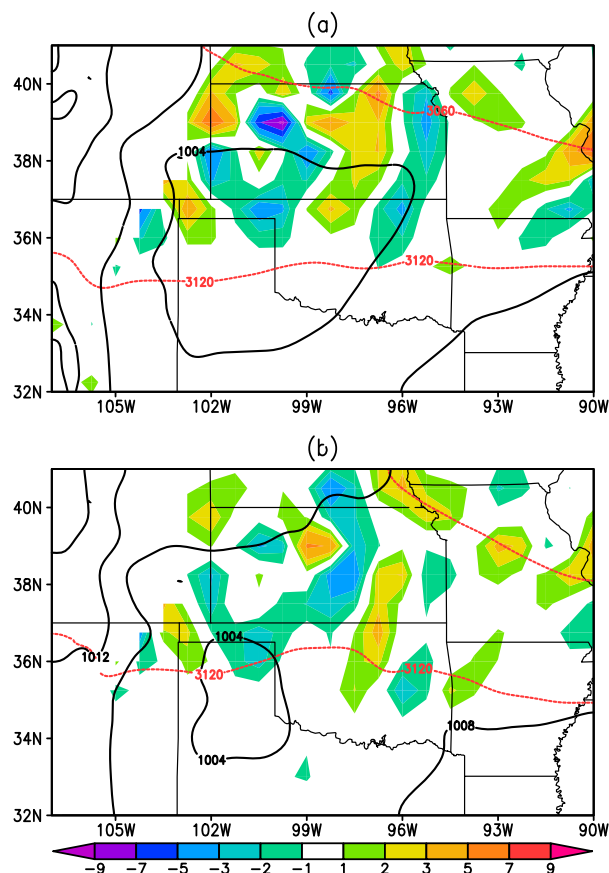
FIG. 11. 700-hPa **Q**-vector convergence ($\times 10^{-11}$ Pa m^{-2} s^{-1}, color shaded), 500-hPa geopotential height (m, red dashed), and sea level pressure (hPa, black contour) for (a) STRONG and (b) WEAK at 0600 UTC 8 May 2009. Negative shaded values denote **Q**-vector convergence.

were analyzed and found to produce qualitatively similar results (not shown). A deeper upstream trough is associated with a stronger 850-hPa circulation 6 h later. By inference, the 500-hPa cyclonic vorticity collocated with the trough is stronger, acting to increase the differential cyclonic vorticity advection over eastern Colorado and western Kansas. Here, a lower-tropospheric warm front stretches east-northeast across southern Kansas from a surface low in the Oklahoma Panhandle, as illustrated by Fig. 9c of Coniglio et al. (2011). From the Pettersen–Sutcliffe development equation [Eq. (8.10) in Carlson (1998)], increasing the magnitude of differential cyclonic vorticity advection in proximity to the baroclinic zone results in stronger leeside synoptic-scale cyclogenesis.

An amplified 500-hPa trough causes numerous alterations to the mesoscale environment. The 850-hPa meridional wind maximum, or LLJ, is strengthened in consequence of a stronger zonal 850-hPa geopotential height gradient that results from stronger leeside

cyclogenesis. The LLJ, which stretches from western Texas into Kansas, is intensified and expanded into western and northern Oklahoma (Fig. 6b). In turn, a stronger circulation is associated with greater 850-hPa specific humidity, presumably resulting from stronger poleward moisture advection, in western and central Kansas (Fig. 6c). Likewise, a stronger circulation is associated with strengthened 850-hPa thermal advection where higher values of potential temperature are shifted northward into southern Kansas (Fig. 6d). The potential temperature gradient associated with the warm front is thus increased. The previous two factors result in a more favorable environment for deep, organized convection in western and central Kansas, as a stronger circulation is associated with larger values of MUCAPE in the southern half of Kansas 6 h before the reference time of 1200 UTC 8 May 2009 (Fig. 6e). Furthermore, increased low-level convergence is found at the nose of the strengthened LLJ, as inferred from Fig. 6b, and acts to promote a stronger meridional potential temperature gradient at the LLJ's nose. In consequence, the LLJ ascends over this frontal zone more rapidly in members with stronger mesovortices under the assumption of isentropic flow. This strengthened ascent could aid CI, following Coniglio et al. (2011).

A sharper meridional potential temperature gradient across Kansas is associated with a stronger front. In turn, this implies stronger cross-frontal cyclonic horizontal wind shear. Consequently, less positive 850-hPa u winds in central and northern Kansas (north of the warm front) and more positive 850-hPa u winds in southern Kansas and northern Oklahoma (south of the warm front) are associated with a stronger circulation (Fig. 6f). This increases the cyclonic horizontal shear across the front and thus the cyclonic relative vorticity associated with the front. Thus, for ensemble members with a stronger circulation, more cyclonic relative vorticity exists in the background environment prior to MCS formation. Weisman et al. (2013) noted that no appreciable background vertical vorticity existed prior to the MCS's formation; however, Evans et al. (2014) found that selected inflowing trajectories along the baroclinic zone did possess appreciable cyclonic vertical vorticity that could be amplified via updraft stretching on the convective and/or system scales.

d. Composites

Note that all results in this section are at 0600 UTC 8 May 2009 to complement the ESA from the previous section. At 500 hPa, STRONG (Fig. 7a) has a slightly more amplified trough as compared to WEAK (Fig. 7b), evidenced by the negative 500-hPa geopotential height differences over the mountain west in Fig. 7c. In turn,
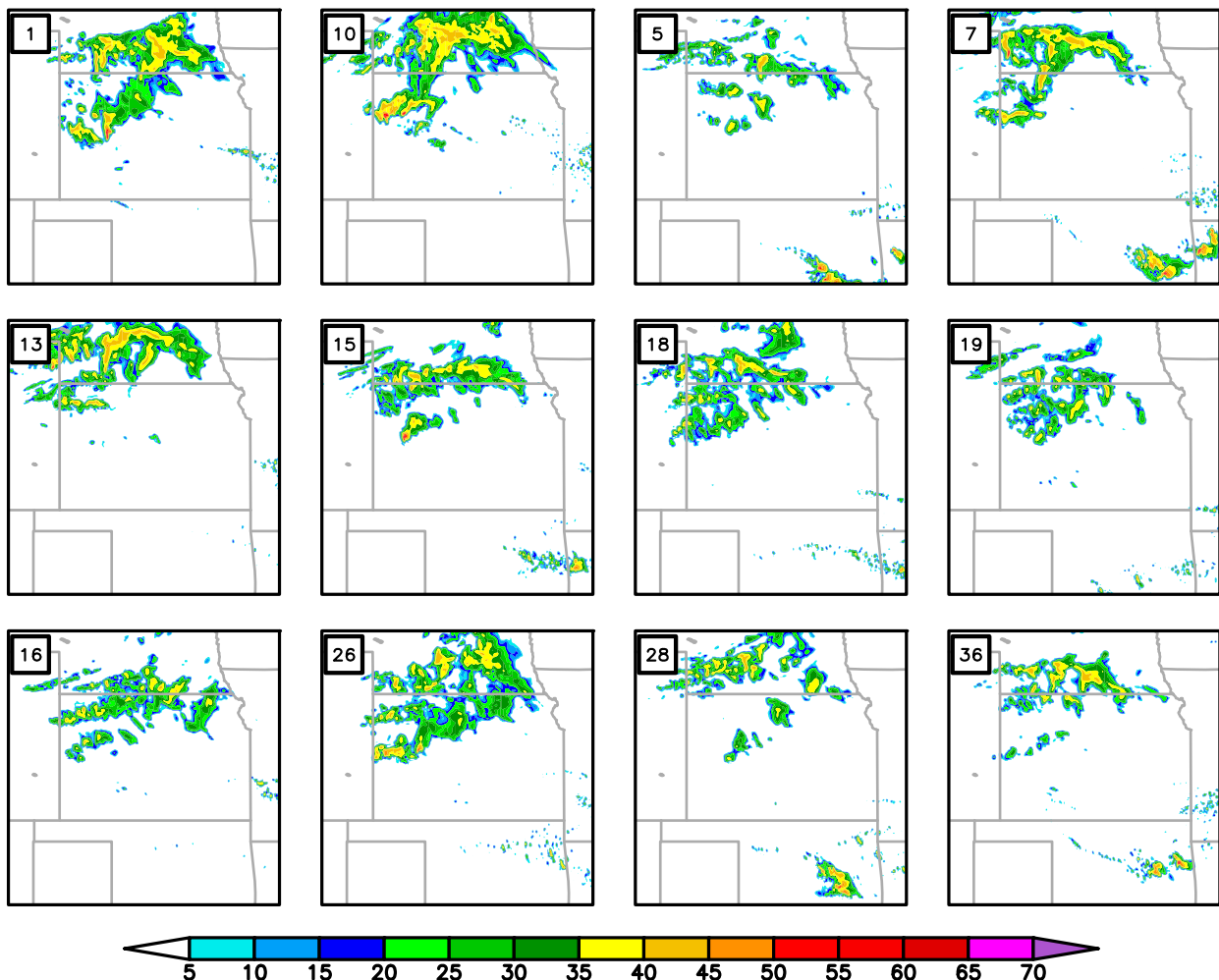
Strong   Weak

FIG. 12. 1-km AGL derived reflectivity (dBZ) at 0600 UTC 8 May 2009 for each individual composite member. STRONG (WEAK) members are on the left (right) half.

the LLJ is stronger and more expansive in STRONG (Fig. 8a) compared to WEAK (Fig. 8b). The enhanced LLJ in STRONG relative to WEAK acts to advect more low-level moisture poleward (Figs. 9a,b). Stronger potential temperature advection across western Kansas is also noted in STRONG (Fig. 9a) as compared to WEAK (Fig. 9b). Figure 9c displays that greater low-level moisture and potential temperature is present over much of Kansas and northern Oklahoma in STRONG. The higher potential temperature results in a stronger meridional potential temperature gradient in STRONG (Fig. 9a) compared to WEAK (Fig. 9b). In turn, greater MUCAPE and reduced most unstable convective inhibition (MUCIN) are found across western Kansas in STRONG (Fig. 10a) as compared to WEAK

(Figs. 10b,c). This implies that WEAK's members will need stronger forced ascent in order to supply the necessary lift to overcome the greater MUCIN and support CI. Generally speaking, STRONG composite mean fields for each variable considered more closely resemble the corresponding 0-h RUC analysis than do WEAK composite mean fields for each variable (not shown).

Plotted **Q**-vector divergence at 700 hPa displays a region of **Q**-vector convergence, implying forcing for upward vertical motion, in northwest Kansas for STRONG (Fig. 11a) relative to the surrounding region. WEAK, on the other hand, has a much weaker signal of forcing for upward vertical motion (Fig. 11b) in the same region. For STRONG members, sustained CI primarily
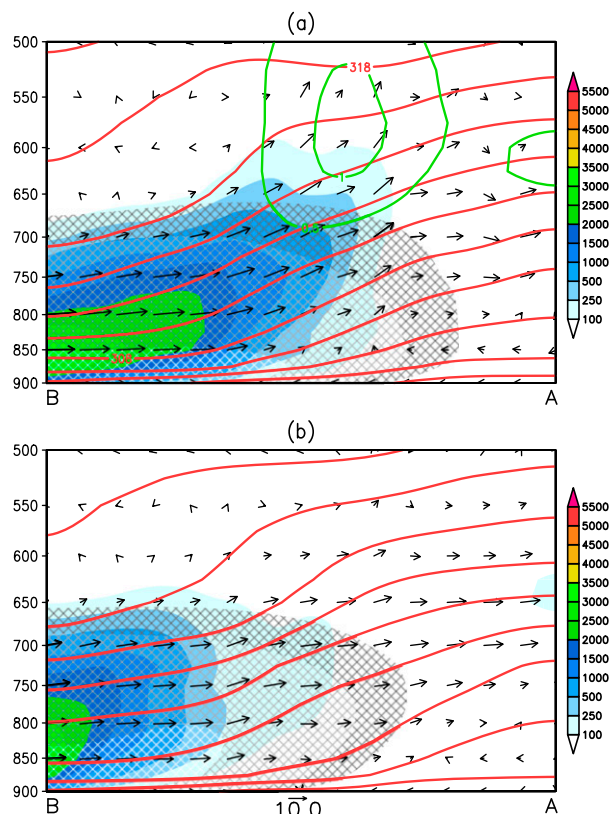
FIG. 13. Plotted vertical cross section of CAPE (J kg^{-1}, color shaded), CIN [J kg^{-1}, gray hatched (white: -100 J kg^{-1}, light gray: -25 J kg^{-1}, dark gray: -10 J kg^{-1})], v–w wind (m s^{-1}, vectors; w is multiplied by 20), isentropes (K, red contour), and cloud water mixing ratio (kg kg^{-1}, green contour) from A–B in Fig. 10 for (a) STRONG and (b) WEAK. The vertical axis is in units of hPa and the time is 0600 UTC 8 May 2009.

occurred within the region of stronger **Q**-vector convergence (Fig. 12) whereas CI occurred in a majority of weak members 1–2 h later to the southeast in southern Kansas and northern Oklahoma (not shown). The STRONG members most closely resemble the observed event (Coniglio et al. 2011) with primary CI in northwestern Kansas. However, secondary CI did occur in southern Kansas a few hours later in the observed event along the baroclinic zone (e.g., Fig. 1 of Coniglio et al. 2011). This is secondary CI in STRONG, but represents the primary CI event in WEAK.

Vertical cross sections were utilized to identify differences between STRONG and WEAK that may have led to the contrast in primary CI. The cross sections stretched meridionally from southwest Kansas to southwest Nebraska along the axes depicted in Fig. 10, from 900 to 500 hPa in the vertical, and are averaged over ±5 grid points in the zonal direction. In STRONG, ascent is noted where the LLJ impinges upon the

baroclinic zone in central Kansas (Fig. 13a). Below 650 hPa to the south, the environment is characterized by large CAPE and CIN. However, to the north, a tongue of CAPE with minimal CIN is located above 650 hPa within the region of isentropic ascent as well as large-scale forcing for ascent [e.g., differential cyclonic vorticity advection (not shown) and **Q**-vector divergence (Fig. 11a)]. Within and above this layer of positive buoyancy, a region of high cloud water mixing ratio exists, signaling the likely presence of convection (as seen in Fig. 12). Conversely, WEAK is associated with lesser CAPE, greater CIN, and reduced ascent (Fig. 13b). Consequently, CI does not occur in western Kansas. This is evidenced by the lack of simulated composite reflectivity values ≥35–40 dB*Z* (Fig. 12), consistent with previous studies in which a minimum reflectivity threshold was used, in whole or in part, to define deep, moist convection from model data and/or observations (e.g., Gremillion and Orville 1999; Kain et al. 2013; Burghardt et al. 2014; Jirak et al. 2014). Similar results were obtained for earlier times (not shown).

For this case, an accurate prediction of the primary CI event may be crucial to mesovortex formation, consistent with Hawblitzel et al. (2007), Schumacher et al. (2013), and Schumacher (2015) that demonstrated MCS and/or mesoscale convective vortex sensitivity to the accurate prediction of CI. We hypothesize that the earlier occurrence of the primary CI event allows the ascending front-to-rear flow, descending rear-to-front flow, and divergent low-level flow, or characteristic airstreams (Houze et al. 1989), of an MCS to develop and mature by the time the simulated (and observed) events passed from Kansas into Missouri. Evans et al. (2014) implicated these airstreams in mesovortex formation. This hypothesis is tested in section 3e with the aid of a circulation budget analysis, as described in section 2e.

e. Circulation budget analysis

At 0800 UTC, member 5 (hereafter MEM5; Fig. 14a) has not developed an MCS, evidenced by the lack of upward vertical motion and strong cyclonic absolute vorticity. However, member 10 (hereafter MEM10; Fig. 14d) does have an organized MCS and a strip of strong cyclonic absolute vorticity along the leading line. By 1000 UTC, MEM5 (Fig. 14b) has developed a MCS, but the storm-relative wind exhibits much weaker 850-hPa rotational and convergent flow around and within the circulation analysis box, respectively, than MEM10 (Fig. 14e). The strip of strong cyclonic absolute vorticity along the leading line of the MCS has also elongated in MEM10 (Fig. 14e) whereas MEM5's cyclonic absolute vorticity is weaker and less expansive (Fig. 14b). In
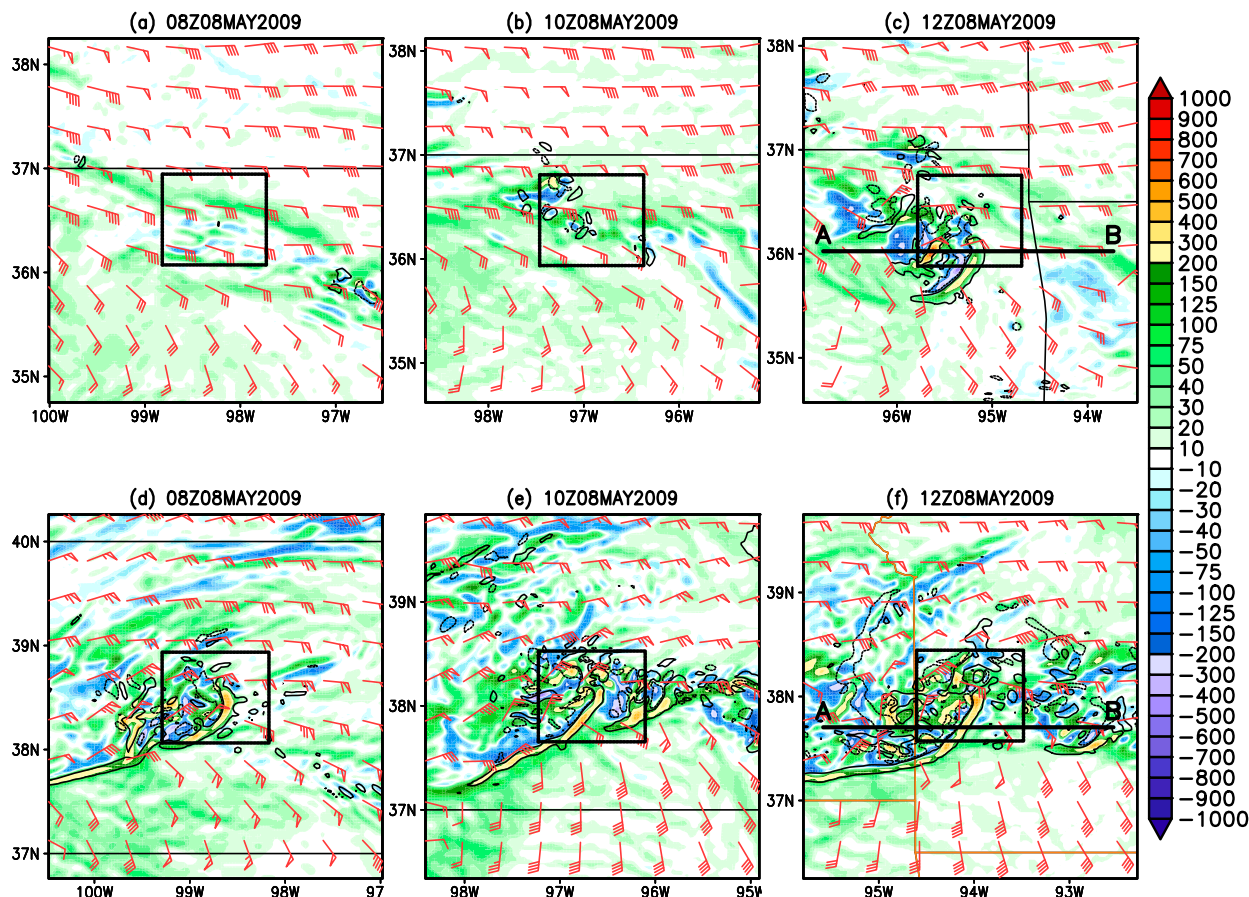
FIG. 14. 850-hPa absolute vorticity ($\times 10^{-5}$ s^{-1}, color shaded), vertical motion (contoured at ± 1 m s^{-1} with negative values dashed), and 850-hPa storm-relative wind (red) (half barb: 5 kt, full barb: 10 kt, pennant: 50 kt) at (a),(d) 0800; (b),(e) 1000; and (c),(f) 1200 UTC 8 May 2009 for (top) MEM5 and (bottom) MEM10. Storm-relative wind is computed with respect to a constant storm motion of (18.4, 2.9) m s^{-1} for MEM5 and (26.9, -2.7) m s^{-1} for MEM10. The black outlined box denotes the control box used in the circulation budget analysis.

MEM10, diffluent outflow (associated with the descending rear-inflow jet) is noted behind the leading line of the MCS (Fig. 14e) while none is present in MEM5 (Fig. 14b). At 1200 UTC, a short strip of cyclonic absolute vorticity is evident along the MCS's leading line in MEM5 and the storm-relative inflow winds have strengthened (Fig. 14c). MEM10's 850-hPa cyclonic absolute vorticity and rotational flow field have not experienced any significant changes since 1000 UTC (Fig. 14f). However, the diffluent outflow rearward and magnitude of the near-storm-relative inflow have increased. A vertical cross section oriented zonally through the MCS at 1200 UTC (Fig. 15) displays that the characteristic airstreams of a MCS are clearer in MEM10 as compared to MEM5. MEM10 (Fig. 15b) has slightly stronger diffluent outflow and stronger storm-relative inflow within the MCS's cold pool and ambient preconvective environment, respectively, compared to MEM5 (Fig. 15a). The characteristic airstreams

of a MCS are believed to be crucial for the convergence of background cyclonic vorticity, as described by Evans et al. (2014). Thus, the three-dimensional airstreams within MEM10 are able to more readily converge background cyclonic absolute vorticity so as to lead to mesovortex development.

The balance between the simulated and budget-predicted temporal change in area-averaged absolute vorticity for MEM5 and MEM10 (Fig. 16) is examined to ensure that budget-predicted circulation changes are faithful representations of simulated circulation changes. Below 850 hPa, the residual does not display a consistent behavior for either MEM5 (Fig. 16c) or MEM10 (Fig. 16d). This contrasts with Fig. 11 of Evans et al. (2014) where the budget-predicted change was consistently greater below 850 hPa, which they argued was likely due to the omission of friction within the budget formulation. Above 850 hPa, no large discrepancies between the simulated and budget-predicted
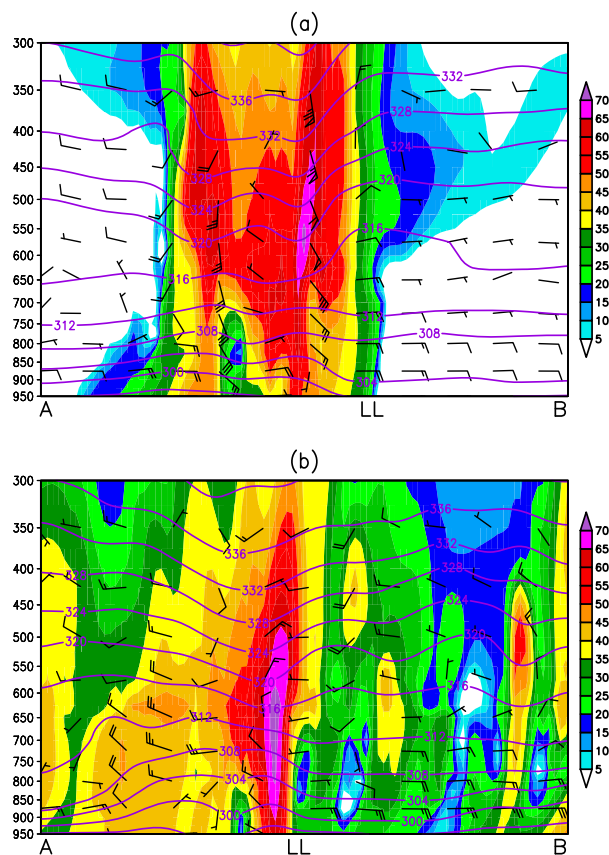
FIG. 15. Plotted vertical cross section of simulated reflectivity (dBZ, color shaded), storm-relative horizontal velocity (v_h) and w (w is multiplied by 3; black) (half barb: 5 kt, full barb: 10 kt, pennant: 50 kt), and isentropes (K, purple contour) from A–B in Fig. 14c for (a) MEM5 and in Fig. 14f for (b) MEM10. The vertical axis is in units of hPa and the time is 1200 UTC 8 May 2009. Storm-relative wind is computed with respect to a constant u storm motion of 18.4 m s^{-1} for MEM5 and 26.9 m s^{-1} for MEM10. "LL" denotes the leading line of the MCS.

temporal change in area-averaged absolute vorticity exist for MEM5 (Fig. 16c). However, for MEM10 (Fig. 16d), the simulated temporal change is greater than the budget prediction from 550–450 to 700–650 hPa between 0800–0900 and 1015–1045 UTC, respectively, the reasons for which are not immediately clear. Additionally, the simulated temporal change is less than the budget-predicted temporal change above 450 hPa between 1000 and 1100 UTC. Nevertheless, there exists strong qualitative and, at times, quantitative agreement between the simulated and budget-predicted changes in area-averaged absolute vorticity for both MEM5 and MEM10.

Figure 17 depicts changes in area-averaged absolute vorticity due to the instantaneous contributions for the sum of all budget forcing terms for MEM5 (Figs. 17a–d) and MEM10 (Figs. 17e–h). For MEM5, the mean

transport of mean planetary vorticity acts to increase the mid- to upper-tropospheric cyclonic area-averaged absolute vorticity after 0900 UTC (Fig. 17a). Conversely, a low- to midtropospheric increase in cyclonic area-averaged absolute vorticity is shown for MEM10 (Fig. 17e) prior to 1200 UTC. MEM10's increased convergent 850-hPa flow into the analysis box at 0800 UTC (Fig. 14d), associated with the trailing dryline, stronger LLJ, and stronger zonal lower-tropospheric baroclinic zone, initially contributes to the greater contribution from the mean transport of planetary vorticity forcing term. The convergent flow associated with the nascent mesovortex dominates the contribution from the mean transport of planetary vorticity forcing term at later times (Figs. 14e,f). The temporal evolution of this forcing term compares well to Evans et al. (2014, their Fig. 13b), with each resulting in a steady increase in area-averaged lower-tropospheric cyclonic absolute vorticity. The inferred vertical profile of convergence within MEM10 suggests a stratiform heating profile, consistent with MCV formation (e.g., Raymond and Jiang 1990). A weak increase in low- to midtropospheric cyclonic area-averaged absolute vorticity is provided by the mean transport of relative vorticity from 0900 to 1130 UTC and after 1400 UTC for MEM5 (Fig. 17b). On the other hand, MEM10 has a very strong low- to midtropospheric increase of area-averaged cyclonic absolute vorticity between 0730 and 1100 UTC (Fig. 17f). The difference between MEM5 and MEM10 for the mean transport of relative vorticity is due to convergent flow into the box with net cyclonic rotation around the box perimeter in MEM10, but not MEM5 (Fig. 14).

In the lower-troposphere, vortex-scale tilting contributes to decreased area-averaged cyclonic absolute vorticity after 1000 UTC for MEM5 (Fig. 17c). In the mid- to upper troposphere, a decrease of area-averaged cyclonic absolute vorticity also occurs due to vortex-scale tilting between 1030 and 1400 UTC. However, the contribution from vortex-scale tilting in the mid- to upper troposphere reverses after 1400 UTC, when it contributes to increased area-averaged cyclonic absolute vorticity. Similarly, MEM10 (Fig. 17g) is characterized by a strong lower-tropospheric decrease and mid- to upper-tropospheric increase of area-averaged cyclonic absolute vorticity due to vortex-scale tilting from 0700–1000 to 1000–1200 UTC, respectively. MEM10's (Figs. 14d–f) simulated MCS was stronger and more organized compared to MEM5 (Figs. 14a–c), presumably allowing for MEM10's descending rear-to-front flow and ascending front-to-rear flow to more strongly influence the vortex-scale tilting term's contribution to the area-averaged cyclonic absolute vorticity (not shown). MEM10 also displays better overall agreement with Evans et al.
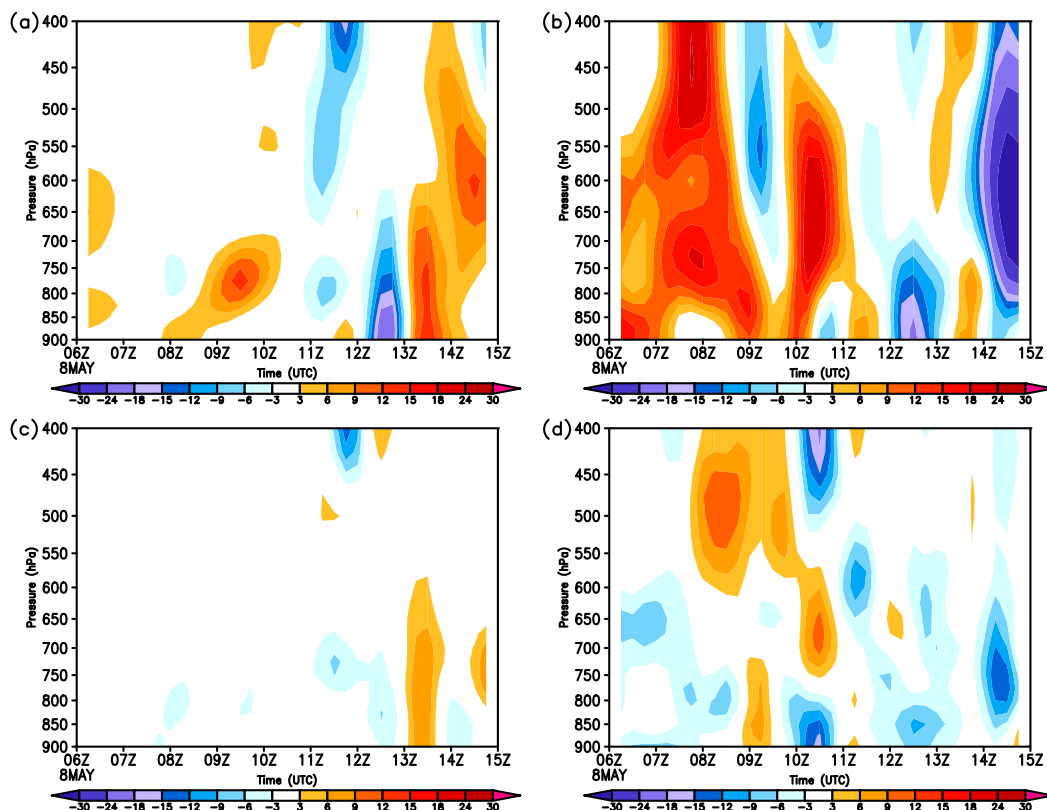
FIG. 16. The (a),(b) simulated temporal change of area-averaged absolute vorticity calculated from dC/dt and (c),(d) residual from the simulated and predicted change of area-averaged absolute vorticity for (left) MEM5 and (right) MEM10. In (c),(d), negative (positive) values denote that the simulated area-averaged absolute vorticity tendency is less (more) cyclonic than the predicted area-averaged absolute vorticity tendency. The time period and isobaric levels for all plots range from 0600 to 1500 UTC 8 May 2009 and 900–400 hPa, respectively. Each panel has units of $\times 10^{-5}\,s^{-1}\,h^{-1}$.

(2014; cf. our Fig. 17g to their Fig. 12c). Eddy transport of perturbation relative vorticity most notably contributes to increased area-averaged cyclonic absolute vorticity between 700 and 575 hPa prior to 0800 UTC and below 700 hPa from 1300 to 1500 UTC for MEM5 (Fig. 17d). However, a decrease of area-averaged cyclonic absolute vorticity is present below 550 hPa from 1200 to 1300 UTC. Contrastingly, MEM10 (Fig. 17h) is characterized by a strong upper-tropospheric increase of area-averaged cyclonic absolute vorticity and a strong low- to midtropospheric decrease from 0700 to 0900 UTC and after 1030 UTC, respectively.

Comparing MEM5 and MEM10 to the results of Evans et al. (2014, their Fig. 12), MEM10 offers the most agreement. However, MEM10's forcing contributions are of greater magnitude and the contribution from eddy transport of perturbation relative vorticity to circulation changes is, overall, out-of-phase with that of Evans et al. (2014; cf. our Fig. 17h to their Fig. 12d). The eddy import of relative vorticity along the zonally oriented baroclinic zone is a primary contributor for an increased 850-hPa

mesovortex associated circulation in MEM10 (not shown). This contrasts with Evans et al. (2014, their Fig. 15a), where the local export of baroclinically generated anticyclonic vertical vorticity within the simulated MCS's cold pool contributed most strongly to positive circulation tendency through the eddy transport term. The convergence of cyclonic absolute vorticity leads to the development of the mesovortex in MEM10 and, to some extent, the simulation analyzed by Evans et al. (2014). We hypothesize that the earlier development of the MCS in MEM10 allows for the airstreams responsible for this forcing to develop earlier while the development of the airstreams is delayed in MEM5 due to the later MCS development.

4. Summary and future work

This research examined the predictability and dynamics of the warm-core mesovortex associated with the 8 May 2009 "super derecho" event. The strength of the upstream upper-level trough is argued to have had an
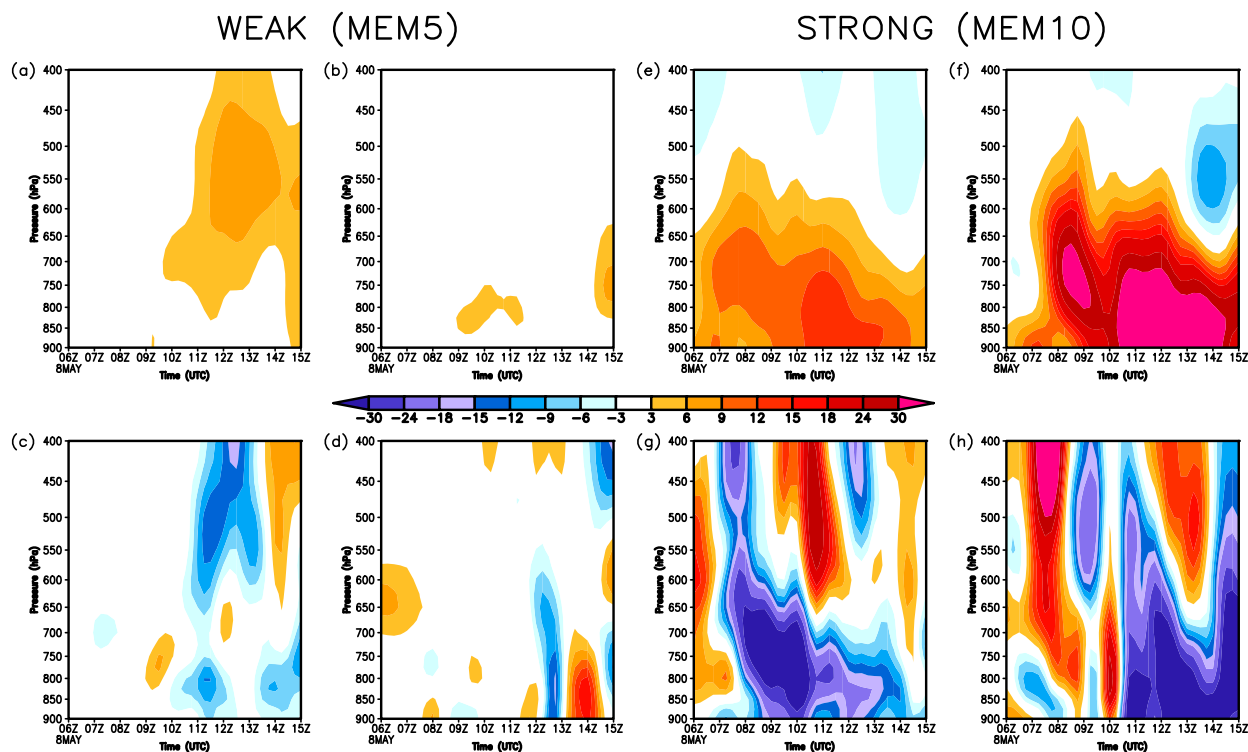
FIG. 17. The (a),(e) stretching of mean planetary vorticity; (b),(f) stretching of mean relative vorticity; (c),(g) tilting of horizontal vorticity; and (d),(h) eddy transport of perturbation relative vorticity forcing contributions to the temporal change in area-averaged absolute vorticity for (a)–(d) MEM5 and (e)–(h) MEM10. Positive values in all fields denote forcing for increased area-averaged absolute vorticity and, by extension, circulation. All fields are for 0600–1500 UTC 8 May 2009 and 900–400 hPa. Each panel has units of $\times 10^{-5}\,\mathrm{s}^{-1}\,\mathrm{h}^{-1}$.

impact on the strength of the 850-hPa circulation associated with the mesovortex, with a more amplified trough being associated with a stronger circulation. The amplified trough resulted in a stronger meridional LLJ over the Texas and Oklahoma Panhandles, a stronger baroclinic zone over Kansas, and stronger horizontal moisture and temperature advection into western Kansas. A circulation budget analysis for the member with the strongest (MEM10) and member with the weakest (MEM5) 850-hPa mesovortex associated circulation revealed that the characteristic airstreams of a MCS were more prominent in MEM10. This allowed for the convergence of more background cyclonic absolute vorticity, facilitating the development of a stronger mesovortex.

All ensemble members simulated an MCS, albeit with substantial differences in when and where the CI event that led to MCS formation occurred. Members with the strongest 850-hPa mesovortex associated circulations forecast the primary CI event in northwest Kansas, resembling the observed event (Coniglio et al. 2011) more closely than did the members with the weakest circulations, in which the primary CI event instead occurred in south-central Kansas. For this event and experimental

setup, the practical predictability is high for MCS occurrence but less with regard to MCS location and strength. Higher practical predictability is displayed in Missouri and Arkansas but is lesser in Kansas (e.g., Figs. 14a,d) signaling how small IC uncertainties and model error can substantially influence the forecasts. Additionally, only 14% of the members produced a feature akin to the observed warm-core mesovortex. Thus, practical predictability is also low for mesovortex formation.

Reducing analysis error magnitude would, in theory, lead to increased mesovortex practical predictability so long as it results in an improved fit of the ensemble analysis to the "true" multiscale attractor(s) for the event. However, as previously mentioned, Melhauser and Zhang (2012) found that a bifurcation point can be reached, at least for some events, such that further analysis error reduction will not lead to forecast improvement. The bifurcation point for this case, should one exist, could lie between a mesovortex and no mesovortex solution without any middle ground. Durran and Weyn (2016) showed that numerical squall-line forecasts could be more skillful if the large-scale initial perturbations were reduced by a small amount rather

than by employing larger reductions to smaller-scale perturbations. Here, the timing of the CI event that leads to initial MCS development appears to significantly affect the development of the mesovortex. Thus, reducing the large-scale errors could have the potential to improve the CI forecast and, in turn, possibly improve the mesovortex forecast. Numerical model performance with regard to CI has been the subject of many research papers (e.g., Lee et al. 1991; Wilson and Roberts 2006; Loftus et al. 2008; Duda and Gallus 2013; Kain et al. 2013; Burghardt et al. 2014), with CI sensitive to a number of factors including perturbations to thermodynamic (Lee et al. 1991) and kinematic fields (Crook 1996) of similar magnitude to observational uncertainty. Future work is necessary to determine the extent to which reducing large-scale or small-scale errors improves CI forecasts for the case studied herein. Further study should also be conducted by testing the scales and magnitudes at which IC uncertainty is implemented and whether a bifurcation point between ensemble member forecasts exists.

REFERENCES

Adams-Selin, R. D., S. C. van den Heever, and R. H. Johnson, 2013: Sensitivity to bow-echo simulation to microphysical parameterizations. *Wea. Forecasting*, **28**, 1188–1209, doi:10.1175/WAF-D-12-00108.1.

Ancell, B., and G. J. Hakim, 2007: Comparing adjoint- and ensemble-sensitivity analysis with applications to observation targeting. *Mon. Wea. Rev.*, **135**, 4117–4134, doi:10.1175/2007MWR1904.1.

Anderson, J. L., 2001: An ensemble adjustment Kalman filter for data assimilation. *Mon. Wea. Rev.*, **129**, 2884–2903, doi:10.1175/1520-0493(2001)129<2884:AEAKFF>2.0.CO;2.

——, 2009: Spatially and temporally varying adaptive covariance inflation for ensemble filters. *Tellus*, **61A**, 72–83, doi:10.1111/j.1600-0870.2008.00361.x.

——, 2012: Localization and sampling error correction in ensemble Kalman filter data assimilation. *Mon. Wea. Rev.*, **140**, 2359–2371, doi:10.1175/MWR-D-11-00013.1.

——, T. Hoar, K. Raeder, H. Liu, N. Collins, R. Torn, and A. Avellano, 2009: The Data Assimilation Research Testbed: A community facility. *Bull. Amer. Meteor. Soc.*, **90**, 1283–1296, doi:10.1175/2009BAMS2618.1.

Barker, D. M., and Coauthors, 2012: The Weather Research and Forecasting Model's Community Variational/Ensemble Data Assimilation System: WRFDA. *Bull. Amer. Meteor. Soc.*, **93**, 831–843, doi:10.1175/BAMS-D-11-00167.1.

Bednarczyk, C. N., and B. C. Ancell, 2015: Ensemble sensitivity analysis applied to a Southern Plains convective event. *Mon. Wea. Rev.*, **143**, 230–249, doi:10.1175/MWR-D-13-00321.1.

Benjamin, S. G., and Coauthors, 2004: An hourly assimilation–forecast cycle: The RUC. *Mon. Wea. Rev.*, **132**, 495–518, doi:10.1175/1520-0493(2004)132<0495:AHACTR>2.0.CO;2.

Berner, J., S.-Y. Ha, J. P. Hacker, A. Fournier, and C. Snyder, 2011: Model uncertainty in a mesoscale ensemble prediction system: Stochastic versus multiphysics representations. *Mon. Wea. Rev.*, **139**, 1972–1995, doi:10.1175/2010MWR3595.1.

Burghardt, B. J., C. Evans, and P. J. Roebber, 2014: Assessing the predictability of convection initiation in the High Plains using an object-based approach. *Wea. Forecasting*, **29**, 403–418, doi:10.1175/WAF-D-13-00089.1.

Carlson, T. N., 1998: *Mid-Latitude Weather Systems*. Amer. Meteor. Soc., 507 pp.

Chen, F., and J. Dudhia, 2001: Coupling an advanced land surface-hydrology model with the Penn State–NCAR MM5 modeling system. Part I: Model implementation and sensitivity. *Mon. Wea. Rev.*, **129**, 569–585, doi:10.1175/1520-0493(2001)129<0569:CAALSH>2.0.CO;2.

Coniglio, M. C., D. J. Stensrud, and M. B. Richman, 2004: An observational study of derecho-producing convective systems. *Wea. Forecasting*, **19**, 320–337, doi:10.1175/1520-0434(2004)019<0320:AOSODC>2.0.CO;2.

——, S. F. Corfidi, and J. S. Kain, 2011: Environment and early evolution of the 8 May 2009 derecho-producing convective system. *Mon. Wea. Rev.*, **139**, 1083–1102, doi:10.1175/2010MWR3413.1.

——, J. Correia Jr., P. T. Marsh, and F. Kong, 2013: Verification of convection-allowing WRF Model forecasts of the planetary boundary layer using sounding observations. *Wea. Forecasting*, **28**, 842–862, doi:10.1175/WAF-D-12-00103.1.

Crook, N. A., 1996: Sensitivity of moist convection forced by boundary layer processes to low-level thermodynamic fields. *Mon. Wea. Rev.*, **124**, 1767–1785, doi:10.1175/1520-0493(1996)124<1767:SOMCFB>2.0.CO;2.

Davis, C. A., and T. J. Galarneau Jr., 2009: The vertical structure of mesoscale convective vortices. *J. Atmos. Sci.*, **66**, 686–704, doi:10.1175/2008JAS2819.1.

Dowell, D. C., F. Zhang, L. J. Wicker, C. Snyder, and N. A. Crook, 2004: Wind and temperature retrievals in the 17 May 1981 Arcadia, Oklahoma, supercell: Ensemble Kalman filter experiments. *Mon. Wea. Rev.*, **132**, 1982–2005, doi:10.1175/1520-0493(2004)132<1982:WATRIT>2.0.CO;2.

Duda, J. D., and W. A. Gallus Jr., 2013: The impact of large-scale forcing on skill of simulated convective initiation and upscale evolution with convection-allowing grid spacings in the WRF. *Wea. Forecasting*, **28**, 994–1018, doi:10.1175/WAF-D-13-00005.1.

Durran, D. R., and M. Gingrich, 2014: Atmospheric predictability: Why butterflies are not of practical importance. *J. Atmos. Sci.*, **71**, 2476–2488, doi:10.1175/JAS-D-14-0007.1.

——, and J. A. Weyn, 2016: Thunderstorms do not get butterflies. *Bull. Amer. Meteor. Soc.*, **97**, 237–243, doi:10.1175/BAMS-D-15-00070.1.

Evans, C., M. L. Weisman, and L. F. Bosart, 2014: Development of an intense, warm-core mesoscale vortex associated with the 8 May 2009 "super derecho" convective event. *J. Atmos. Sci.*, **71**, 1218–1240, doi:10.1175/JAS-D-13-0167.1.

Gaspari, G., and S. E. Cohn, 1999: Construction of correlation functions in two and three dimensions. *Quart. J. Roy. Meteor. Soc.*, **125**, 723–757, doi:10.1002/qj.49712555417.

Gremillion, M. S., and R. E. Orville, 1999: Thunderstorm characteristics of cloud-to-ground lightning at the Kennedy Space Center, Florida: A study of lightning initiation signatures as indicated by the WSR-88D. *Wea. Forecasting*, **14**, 640–649, doi:10.1175/1520-0434(1999)014<0640:TCOCTG>2.0.CO;2.

Ha, S.-Y., and C. Snyder, 2014: Influence of surface observations in mesoscale data assimilation using an ensemble Kalman filter. *Mon. Wea. Rev.*, **142**, 1489–1508, doi:10.1175/MWR-D-13-00108.1.

Hawblitzel, D. P., F. Zhang, Z. Meng, and C. A. Davis, 2007: Probabilistic evaluation of the dynamics and predictability of the mesoscale convective vortex of 10–13 June 2003. *Mon. Wea. Rev.*, **135**, 1544–1563, doi:10.1175/MWR3346.1.

Hohenegger, C., and C. Schar, 2007: Predictability and error growth dynamics in cloud-resolving models. *J. Atmos. Sci.*, **64**, 4467–4478, doi:10.1175/2007JAS2143.1.

——, D. Luthi, and C. Schar, 2006: Predictability mysteries in cloud-resolving models. *Mon. Wea. Rev.*, **134**, 2095–2107, doi:10.1175/MWR3176.1.

Houtekamer, P. L., and H. L. Mitchell, 1998: Data assimilation using an ensemble Kalman filter technique. *Mon. Wea. Rev.*, **126**, 796–811, doi:10.1175/1520-0493(1998)126<0796:DAUAEK>2.0.CO;2.

Houze, R. A., Jr., M. I. Biggerstaff, S. A. Rutledge, and B. F. Smull, 1989: Interpretation of Doppler weather radar displays of midlatitude mesoscale convective systems. *Bull. Amer. Meteor. Soc.*, **70**, 608–619, doi:10.1175/1520-0477(1989)070<0608:IODWRD>2.0.CO;2.

Iacono, M. J., J. S. Delamere, E. J. Mlawer, M. W. Shephard, S. A. Clough, and W. D. Collins, 2008: Radiative forcing by long-lived greenhouse gases: Calculations with the AER radiative transfer models. *J. Geophys. Res.*, **113**, D13103, doi:10.1029/2008JD009944.

Janjić, Z. I., 1994: The stop-mountain eta coordinate model: Further developments of the convection, viscous sublayer, and turbulence closure schemes. *Mon. Wea. Rev.*, **122**, 927–945, doi:10.1175/1520-0493(1994)122<0927:TSMECM>2.0.CO;2.

Jirak, I. L., C. J. Melick, and S. J. Weiss, 2014: Combining probabilistic ensemble information from the environment with simulated storm attributes to generate calibrated probabilities of severe weather hazards. *27th Conf. on Severe Local Storms*, Madison, WI, Amer. Meteor. Soc., JP2.5. [Available online at https://ams.confex.com/ams/27SLS/webprogram/Paper254649.html.]

Kain, J. S., and Coauthors, 2013: A feasibility study for probabilistic convection initiation forecasts based on explicit numerical guidance. *Bull. Amer. Meteor. Soc.*, **94**, 1213–1225, doi:10.1175/BAMS-D-11-00264.1.

Kuo, Y.-H., T.-K. Wee, S. Sokolovskiy, C. Rocken, W. Schreiner, D. Hunt, and R. A. Anthes, 2004: Inversion and error estimation of GPS radio occultation data. *J. Meteor. Soc. Japan*, **82**, 507–531, doi:10.2151/jmsj.2004.507.

Kursinski, E. R., G. A. Hajj, J. T. Shofield, R. P. Linfied, and K. R. Hardy, 1997: Observing Earth's atmosphere with radio occultation measurements using the Global Positioning System. *J. Geophys. Res.*, **102**, 23 429–23 465, doi:10.1029/97JD01569.

Lawson, J., and W. A. Gallus Jr., 2016: On contrasting ensemble simulations of two Great Plains bow echoes. *Wea. Forecasting*, **31**, 787–810, doi:10.1175/WAF-D-15-0060.1.

Lee, B. D., R. D. Farley, and M. R. Hjelmfelt, 1991: A numerical case study of convection initiation along colliding convergence boundaries in northeast Colorado. *J. Atmos. Sci.*, **48**, 2350–2366, doi:10.1175/1520-0469(1991)048<2350:ANCSOC>2.0.CO;2.

Loftus, A. M., D. B. Weber, and C. A. Doswell III, 2008: Parameterized mesoscale forcing mechanisms for initiating numerically simulated isolated multicellular convection. *Mon. Wea. Rev.*, **136**, 2408–2421, doi:10.1175/2007MWR2133.1.

Melhauser, C., and F. Zhang, 2012: Practical and intrinsic predictability of severe and convective weather at the mesoscales. *J. Atmos. Sci.*, **69**, 3350–3371, doi:10.1175/JAS-D-11-0315.1.

Peters, J. M., and P. J. Roebber, 2014: Synoptic control of heavy-rain-producing convective training episodes. *Mon. Wea. Rev.*, **142**, 2464–2482, doi:10.1175/MWR-D-13-00263.1.

Raymond, W. H., and H. Jiang, 1990: A theory for long-lived mesoscale convective systems. *J. Atmos. Sci.*, **47**, 3067–3077, doi:10.1175/1520-0469(1990)047<3067:ATFLLM>2.0.CO;2.

Romine, G. S., C. S. Schwartz, C. Snyder, J. L. Anderson, and M. L. Weisman, 2013: Model bias in a continuously cycled assimilation system and its influence on convection-permitting forecasts. *Mon. Wea. Rev.*, **141**, 1263–1284, doi:10.1175/MWR-D-12-00112.1.

——, ——, J. Berner, K. R. Fossell, C. Snyder, J. L. Anderson, and M. L. Weisman, 2014: Representing forecast error in a convection-permitting ensemble system. *Mon. Wea. Rev.*, **142**, 4519–4541, doi:10.1175/MWR-D-14-00100.1.

Schumacher, R. S., 2015: Resolution dependence of initiation and upscale growth of deep convection in convection-allowing forecasts of the 31 May–1 June 2013 supercell and MCS. *Mon. Wea. Rev.*, **143**, 4331–4354, doi:10.1175/MWR-D-15-0179.1.

——, A. J. Clark, M. Xue, and F. Kong, 2013: Factors influencing the development and maintenance of nocturnal heavy-rain-producing convective systems in a storm-scale ensemble. *Mon. Wea. Rev.*, **141**, 2778–2801, doi:10.1175/MWR-D-12-00239.1.

Schwartz, C. S., Z. Liu, K. R. Smith, and M. L. Weisman, 2014: Characterizing and optimizing precipitation forecasts from a convection-permitting ensemble initialized by a mesoscale ensemble Kalman filter. *Wea. Forecasting*, **29**, 1295–1318, doi:10.1175/WAF-D-13-00145.1.

——, G. S. Romine, R. A. Sobash, K. R. Fossell, and M. L. Weisman, 2015a: NCAR's experimental real-time convection-allowing ensemble prediction system. *Wea. Forecasting*, **30**, 1645–1654, doi:10.1175/WAF-D-15-0103.1.

——, ——, M. L. Weisman, R. A. Sobash, K. R. Fossell, K. W. Manning, and S. B. Trier, 2015b: A real-time convection-allowing ensemble prediction system initialized by mesoscale ensemble Kalman filter analysis. *Wea. Forecasting*, **30**, 1158–1181, doi:10.1175/WAF-D-15-0013.1.

——, Z. Liu, and X.-Y. Huang, 2015c: Sensitivity of limited-area hybrid variational-ensemble analyses and forecasts to ensemble perturbation resolution. *Mon. Wea. Rev.*, **143**, 3454–3477, doi:10.1175/MWR-D-14-00259.1.

Skamarock, W. C., and Coauthors, 2008: A description of the Advanced Research WRF version 3. NCAR Tech. Note NCAR/TN-475+STR, 113 pp., doi:10.5065/D68S4MVH.

Snively, D. V., and W. A. Gallus Jr., 2014: Prediction of convective morphology in near-cloud-permitting WRF model simulations. *Wea. Forecasting*, **29**, 130–149, doi:10.1175/WAF-D-13-00047.1.

Thompson, G., P. R. Field, R. M. Rasmussen, and W. D. Hall, 2008: Explicit forecasts of winter precipitation using an improved bulk microphysics scheme. Part II: Implementation of a new snow parameterization. *Mon. Wea. Rev.*, **136**, 5095–5115, doi:10.1175/2008MWR2387.1.

Tiedtke, M., 1989: A comprehensive mass flux scheme for cumulus parameterization in large-scale models. *Mon. Wea. Rev.*, **117**, 1779–1800, doi:10.1175/1520-0493(1989)117<1779:ACMFSF>2.0.CO;2.

Torn, R. D., 2010: Performance of a mesoscale ensemble Kalman filter (EnKF) during the NOAA high-resolution hurricane test. *Mon. Wea. Rev.*, **138**, 4375–4392, doi:10.1175/2010MWR3361.1.

——, and G. J. Hakim, 2008: Ensemble-based sensitivity analysis. *Mon. Wea. Rev.*, **136**, 663–677, doi:10.1175/2007MWR2132.1.

——, and G. S. Romine, 2015: Sensitivity of central Oklahoma convection forecasts to upstream potential vorticity anomalies during two strongly forced cases during MPEX. *Mon. Wea. Rev.*, **143**, 4064–4087, doi:10.1175/MWR-D-15-0085.1.

——, G. J. Hakim, and C. Snyder, 2006: Boundary conditions for limited-area ensemble Kalman filters. *Mon. Wea. Rev.*, **134**, 2490–2502, doi:10.1175/MWR3187.1.

Velden, C., and Coauthors, 2005: Recent innovations in deriving tropospheric winds from meteorological satellites. *Bull. Amer. Meteor. Soc.*, **86**, 205–223, doi:10.1175/BAMS-86-2-205.

Wandishin, M. S., D. J. Stensrud, S. L. Mullen, and L. J. Wicker, 2008: On the predictability of mesoscale convective systems: Two-dimensional simulations. *Wea. Forecasting*, **23**, 773–785, doi:10.1175/2008WAF2007057.1.

——, ——, ——, and ——, 2010: On the predictability of mesoscale convective systems: Three-dimensional simulations. *Mon. Wea. Rev.*, **138**, 863–885, doi:10.1175/2009MWR2961.1.

Weisman, M. L., C. Evans, and L. F. Bosart, 2013: The 8 May 2009 superderecho: Analysis of a real-time explicit convective forecast. *Wea. Forecasting*, **28**, 863–892, doi:10.1175/WAF-D-12-00023.1.

——, and Coauthors, 2015: The Mesoscale Predictability Experiment (MPEX). *Bull. Amer. Meteor. Soc.*, **96**, 2127–2149, doi:10.1175/BAMS-D-13-00281.1.

Wilson, J. W., and R. D. Roberts, 2006: Summary of convective storm initiation and evolution during IHOP: Observational and modeling perspective. *Mon. Wea. Rev.*, **134**, 23–47, doi:10.1175/MWR3069.1.

Xu, X., M. Xue, and Y. Wang, 2015a: The genesis of mesovortices within a real-data simulation of a bow echo system. *J. Atmos. Sci.*, **72**, 1963–1986, doi:10.1175/JAS-D-14-0209.1.

——, ——, and ——, 2015b: Mesovortices within the 8 May 2009 bow echo over the central United States: Analyses of the characteristics and evolution based on Doppler radar observations and a high-resolution model simulation. *Mon. Wea. Rev.*, **143**, 2266–2290, doi:10.1175/MWR-D-14-00234.1.

Zhang, C., Y. Wang, and K. Hamilton, 2011: Improved representation of boundary layer clouds over the southeast Pacific in ARW-WRF using a modified Tiedtke cumulus parameterization scheme. *Mon. Wea. Rev.*, **139**, 3489–3513, doi:10.1175/MWR-D-10-05091.1.